Cooper, S. B., Tiels, K., Titurus, B., & Di Maio, D. (2020). Polynomial Nonlinear State Space Identification of an Aero-Engine Structure. *Computers and Structures*, *238*, [106299]. https://doi.org/10.1016/j.compstruc.2020.106299

Peer reviewed version

License (if available):
CC BY-NC-ND

Link to published version (if available):
10.1016/j.compstruc.2020.106299

Link to publication record in Explore Bristol Research
PDF-document

This is the author accepted manuscript (AAM). The final published version (version of record) is available online via Elsevier at https://www.sciencedirect.com/science/article/pii/S0045794920301024. Please refer to any applicable terms of use of the publisher.

University of Bristol - Explore Bristol Research

General rights

This document is made available in accordance with publisher policies. Please cite only the published version using the reference above. Full terms of use are available:
http://www.bristol.ac.uk/red/research-policy/pure/user-guides/ebr-terms/

Polynomial Nonlinear State Space Identification of an Aero-Engine Structure

Samson B.Cooper*[1], Koen Tiels[2], Brano Titurus[1] and Dario DiMaio[1]
[1] University of Bristol, Department of Mechanical Engineering, Queen's Building, University Walk, Bristol, United Kingdom.
[2] Uppsala University, Department of Information Technology, PO Box 337, 75105 Uppsala Sweden.

Abstract

Most nonlinear identification problems often require prior knowledge or an initial assumption of the mathematical law (model structure) and data processing to estimate the nonlinear parameters present in a system, i.e. they require the functional form or depend on a proposition that the measured data obey a certain nonlinear function. However, obtaining prior knowledge or performing nonlinear characterisation can be difficult or impossible for certain identification problems due to the individualistic nature of practical nonlinearities. For example, joints between substructures of large aerospace design frequently feature complex physics at local regions of the structure, making a physically motivated identification in terms of nonlinear stiffness and damping impossible. As a result, black-box models which use no prior knowledge can be regarded as a proficient method, this paper explores the pragmatism of a black-box approach based on Polynomial Nonlinear State Space (PNLSS) models to identify the nonlinear dynamics observed in a large aerospace component. As a first step, the Best Linear Approximation (BLA), noise and nonlinear distortion levels are estimated over different amplitudes of excitation using the Local Polynomial Method (LPM). Next, a linear state space model is estimated on the non-parametric BLA using the frequency domain subspace identification method. Nonlinear model terms are then constructed in the form of multivariate polynomials in the state variables while the parameters are estimated through a nonlinear optimisation routine. Further analyses were also conducted to determine the most suitable monomial degree and type required for the nonlinear identification procedure. Practical application is carried out on an Aero-Engine casing assembly with multiple joints, while model estimation and validation is achieved using measured sine-sweep and broadband data obtained from the experimental campaign.

Keywords: Nonlinear systems; System identification; Black-box model; State-space models and Aircraft structures

1. Introduction

The levels of nonlinearities encountered during the vibration test of aerospace structures is ever increasing and becoming more significant as attested by the literature [1]. Over the last few years, evidence of nonlinear phenomena has been reported during the Ground Vibration Testing (GVT) of large aircraft structures [2-4] and it is now evident that these cases require profound investigation to understand and identify the nonlinearities observed in such test data. In addition, the use of developed linear tools and theories to perform identification on nonlinear test data often produces undesirable results or in most cases fail to predict the structural response within the acceptable levels [5, 6] which are required for validation and industrial certification purpose. Hence the development of effective system identification techniques applicable to nonlinear systems is a major demand by many structural dynamic engineers and researchers.

In most cases, the detection of nonlinearity from measured data can easily be achieved by using simple techniques such as the superposition principle, observation of distorted peaks at the resonances and recognition of jumps between low and high response amplitudes. After nonlinearity has been detected in measured data, identification of parametric or non-parametric models from such data is often a challenging task. The last two decades have witnessed the development of several procedures and methods for nonlinear system identification. These methods can mostly be grouped into three different categories namely white-box [7], black-box [8] and grey-box [9] identification.

Black-box modelling has proven to be a successful way of tackling nonlinear system identification, especially for case studies where the functional forms and mathematical law governing the nonlinearities are challenging to obtain prior to the final parameter estimation. In this case the only available information about the system is given by the measured inputs and outputs. A black-box approach uses model structures that are adequate and rich to capture all the appropriate physics and dynamics governing the nonlinearities of a given system. Examples of black-box models available in the literature are: nonlinear autoregressive network (NARX) and nonlinear autoregressive moving average (NARMAX) with exogenous inputs models [10, 11], the Volterra models [12-14], neural networks [8, 15] and state space models [16-18]. Although, results obtained from black-box models can be challenging to interpret in terms of nonlinear stiffness or damping parameters for the system under investigation, the advantage of their flexible mathematical and model structures can be used to capture significant nonlinear behaviours observed in measured data.

Obtaining a prior knowledge of the nonlinear functional form or nonlinear characteristics of large assembled structures with joints can be very challenging due to their specific nonlinear behaviour such as stick-slip behaviour at macro- and microscopic levels and hysteretic damping behaviour. As such, black-box identification methods are often considered as a reasonable approach to capture relevant information about the characteristics and nature of nonlinearities in the system based on measured input and output data. An emerging black-box modelling method utilised in nonlinear system identification is based on the state space modelling approach. These state space models have a non-specific representation that can be used to model a variety of mechanical and control systems. Most importantly, nonlinear state space models have the flexibility and capacity to capture different types of nonlinear phenomena. Recent work and contributions in this research area including applications are demonstrated in [17, 19-21].

In this paper, a black-box data driven approach based on the Polynomial Nonlinear State Space (PNLSS) model [16] is applied to develop a state-space representation of the measured data and capture relevant nonlinearities observed during the experimental campaign of a large aero-engine casing. In this case, a physical interpretation of the structure under test is not pursued, rather a PNLSS model capable of describing a Single Input Multiple Output (SIMO) representation of the system and its corresponding nonlinearity is developed. A benefit of using state space models is the suitability for modelling a variety of system configurations such as Multiple-Inputs and Multiple-Outputs (MIMO), Single-Input and Multiple-Output (SIMO) and Single Input and Single Output (SISO) systems. The approach adopted in this paper exploits the great flexibility of the PNLSS model to investigate the nonlinear characteristics observed at measured local regions of the structure. Furthermore, a major challenge in black-box modelling or nonlinear experimental identification is the concern between the flexibility of the fitted model and its parsimony [1]. For this study, flexibility is defined here as the ability of the derived model to capture nonlinearities observed across multiple vibration modes while parsimony is the ability for the fitted model to have the lowest possible number of parameters. In this paper, more attention is drawn towards developing a PNLSS model capable of modelling and identifying the nonlinearities observed across three consecutive vibration modes of an aero-engine casing whilst maintaining the lowest number of possible parameters. The PNLSS identification was conducted on measured sine-sweep data, while the validity of the derived model is tested on broadband data.

A preliminary investigation on the effect of nonlinearities was conducted on the test structure with some initial results published in a conference proceeding in [32]. Compared to [32], this paper includes a pre-test analysis with a finite element model, identification in a larger frequency range with more nonlinearly distorted modes, broadband validation experiments, and a study on identifying a suitable parsimonious model. In addition, this paper addresses one of the challenging task of the Highly Innovative Technonlogy Enabler for Aeropsace (HiTEA) research program funded by Innovation UK funding scheme. One of the objective of this project was to design and validate experimental test rig up to Technology Readiness Level 6 (TRL6) capable of being used for smart Structural Health Monitoring (SHM) methods through the integration of experimental test and simulation. This objective required understanding and identifying the effects of nonlinearities triggered by joints and bolted assemblies on an aerospace structure provided by Rolls-Royce. This paper presents results obtained for the nonlinear experimental campaign and identification.

This paper is structured as follows. A brief discussion on black-box identification based on state space modelling is presented in section 2. The entire identification procedure including the implemented techniques such as the Best Linear Approximation (BLA) and the full nonlinear identification based on the Levenberg-Marquardt (LM) algorithm is described in section 3. In section 4, the PNLSS identification is implemented on measured data obtained from a test campaign conducted on an aero-engine casing. A parametric and non-parametric study of the total distortions (noise and nonlinear distortions) observed in the test data are presented. In addition, further analysis on deriving a flexible PNLSS model capable of capturing the observed nonlinearities is presented based on sine-sweep and Frequency Response Function (FRF) data. The validity of the identified model using an independent set of measured sine-sweep and broadband data is tested and illustrated in section 5 while discussions and concluding remarks are presented in section 6.

2. Black-box Identification Based on State Space Models

To identify or model nonlinear systems, one often needs to examine the device under test thoroughly and develop a befitting model using first principles derived from physics and nonlinear dynamics laws [7]. However, developing a fully understood physics-based model is time consuming and sometimes impossible for devices or systems with multiple sources and types of nonlinearities originating from bolted connections and joints as in the case of the aero-engine casing assembly under study. In the present case the only available information about the device under test is the measured inputs and outputs. Considering the nonlinear structure, in this case the aero-engine casing assembly, as a black-box, a flexible data-driven model can be developed to capture the principle nonlinearities without utilising significant physical or internal information about the aero-engine casing assembly.

2.1. State Space Models

A state space representation can conveniently model a system with multiple inputs and multiple outputs [1]. In this case, discrete-time models are adopted as opposed to continuous-time models which are computationally intensive due to calculations of time derivatives and integrals of nonlinear functions. Furthermore, a continuous-time model is not essential when using black-box approach since the estimation of physical parameters is not the main pursuit. A discrete-time state space model in a general form is expressed as:

$$\begin{cases} x(t+1) = f\big(x(t), u(t)\big) \\ \quad y(t) = g\big(x(t), u(t)\big) \end{cases} \tag{1}$$

where $u(t) \in \mathbb{R}^{n_u}$ is a vector containing the n_u input values at time instant t, note that $n_u = 1$ in this study, while $y(t) \in \mathbb{R}^{n_y}$ is the vector of the n_y outputs. The state vector $x(t) \in \mathbb{R}^{n_a}$ represents the memory of the system and stores the collective dynamics present in the different outputs. The first line of equation (1) represents the state equation which describes the evolution of the states as a function of

the inputs and the previous states. The second line of equation (1) is called the output equation and it relates the system's output with the states and the inputs.

Here, the state space model equation will be defined as a classical linear state space model (with state space matrices $A \in \mathbb{R}^{n_a \times n_a}$, $B \in \mathbb{R}^{n_a \times n_u}$, $C \in \mathbb{R}^{n_y \times n_a}$, and $D \in \mathbb{R}^{n_y \times n_u}$) with the addition of nonlinear functions f_{NL} and g_{NL} to the state and output equations. Equation (2) describes a discrete time model of a nonlinear state space model [16].

$$\begin{cases} x(t+1) = Ax(t) + Bu(t) + f_{\mathrm{NL}}(x(t), u(t)) \\ \quad y(t) = Cx(t) + Du(t) + g_{\mathrm{NL}}(x(t), u(t)) \end{cases} \tag{2}$$

The functions f_{NL} and g_{NL} can use a set of basis functions of different types such as wavelets, sigmoid functions, polynomials, hyperbolic tangents, or radial basis functions [16]. In this paper, polynomial nonlinear state space models are selected based on their ability to provide enough flexibility to cover the problem of interest.

2.2. Polynomial Nonlinear State Space Models

In a Polynomial Nonlinear State Space (PNLSS) model, the nonlinear functions f_{NL} and g_{NL} in Eqs (2) are expanded using basis functions by extending the linear state and the output equation with polynomials in the state and the input variable [16]:

$$x(t+1) = Ax(t) + Bu(t) + E\zeta(x(t), u(t)) \tag{3}$$

$$y(t) = Cx(t) + Du(t) + F\eta(x(t), u(t)) \tag{4}$$

where the vectors ζ and η contain all nonlinear monomials with user-chosen degrees larger than one, and the matrices $E \in \mathbb{R}^{n_a \times n_\zeta}$ and $F \in \mathbb{R}^{n_y \times n_\eta}$ contain the corresponding monomial coefficients. The matrices B and D have $n_u = 1$ column for SIMO models, and E and F have a number of columns that corresponds to the total number of monomials of the user-chosen degrees. Nonlinear dynamics is captured through the inclusion of the nonlinear terms $E\,\zeta$ and $F\,\eta$. In particular, assuming a SIMO model, the monomials $\zeta(t)$ and $\eta(t)$ are formed by all possible products of the input and the state variables raised to a chosen degree, e.g. for an element in $\zeta(t)$, [16]

$$\zeta_{k,l_1,\ldots,l_{n_x}}(t) = u^k(t) \prod_{i=1}^{n_a} x_i^{l_i}(t) \tag{5}$$

where the total degree of monomial fulfills the condition: $k + \sum_{i=1}^{n_a} l_i \in \{0,2,3,\ldots,d\}$. Polynomial expansions are useful because they are linear in parameters, hold universal approximation properties, and can easily be extended to multivariate cases [16, 19].

2.3. Model Structure

A data driven nonlinear black-box modelling often requires a flexible model structure capable of representing all the nonlinearities observed in an interested case study. In this paper, the SIMO configuration is used in deriving a data driven nonlinear model for the assembled engine casing.

Although a PNLSS model can capture wide range of nonlinear effects, it is important that an appropriate model structure is selected to reduce and manage the effects of the increasing number of parameters based on a combination of the polynomial degree and number of input and state variables. The model structures considered here are classified as full model and state only model [20]. For a full model structure all elements in the matrices E and F of equations (3) and (4) are taken into consideration during the optimization process, while a state only model structure only considers the elements in $E\zeta(x(t))$ and $F\eta(x(t))$ i.e. no input terms are considered.

For a full PNLSS model where all monomials of degree $d_1, d_2, \dots, d_K$ are present, the number of elements in the matrices E and F combined can be computed using the following expression

$$s = \left(\sum_{i=1}^{K} \frac{(n_a + n_u - 1 + d_i)!}{(n_a + n_u - 1)!\, d_i!} \right) \left(n_a + n_y \right) \tag{6}$$

For a full PNLSS model with consecutive polynomial degrees 2, 3, …, d, the sum in (6) could be worked out explicitly:

$$s_{\text{full}} = \left(\frac{(n_a + n_u + d)!}{(n_a + n_u)!\, d!} - (n_a + n_u) - 1 \right) \left(n_a + n_y \right) \tag{7}$$

The number of terms in a polynomial with $n_a + n_u$ inputs and consecutive degrees 0, 1, …, d is given by $\frac{(n_a+n_u+d)!}{(n_a+n_u)!d!}$. Removing the number of linear terms $(n_a + n_u)$ and constant terms (one) and multiplying with the number of polynomials $(n_a + n_y)$ results in the expression in (7).

For a state only model, the number of parameters is reduced with n_u in (7) being considered to be zero:

$$s_{\text{state}} = \left(\frac{(n_a + d)!}{n_a!\, d!} - n_a - 1 \right) \left(n_a + n_y \right) \tag{8}$$

Solving the governing nonlinear equations of motion for large industrial scale structure with substructures and jointed interfaces can easily become computationally intensive due to the large amount of data processing involved, hence selecting an appropriate model structure is of major importance. Since the main application of this paper is demonstrated on a large aircraft-engine casing, the state only model structure is utilised to reduce the computational burden and the number of parameters during the identification process. The state only model structure is utilised based on the assumptions that there are no nonlinearities observed in the input signal or excitation. This leads to disregarding the input variables in the monomial combinations.

3. Identification Procedure

This section of the paper describes the identification procedure that is implemented for a data driven nonlinear state space model for the casing assembly based on experimental data. The state space identification approach used in this paper is fundamentally based on four different steps. These steps are listed below with a brief description and summarised schematically in Figure 1.

1) To obtain the PNLSS model of a system, it is often beneficial when the initial linear state space parameters (A, B, C, D) of the nonlinear system are identified first. To do this, a non-parametric Best Linear Approximation (BLA) of the system is determined here using the Local Polynomial Method (LPM) [22]. Additionally, an estimate of the total variance (i.e. the sum of the noise and nonlinear variance) is obtained.

2) A linear state space parametric model (A, B, C, D) is identified from the BLA using a frequency domain subspace method [23]. The weighted mean square difference between the estimated FRF of the BLA and the FRF of the linear state space model is minimised. This weighting is used to select a frequency band of interest and is typically the inverse of the total variance estimated in the previous step.

3) The linear state space model is then extended with polynomial terms in the states. The corresponding polynomial coefficients, together with those of the linear state space model are optimised using the Levenberg-Marquardt method [24]. The linear parameters are optimised

again because the initial guess is biased due to nonlinear distortions. Re-estimating the linear coefficients improves the input/output fit. A cost function is defined to minimise the weighted mean square difference between the measured and the modelled output spectra of the Polynomial Nonlinear State Space (PNLSS) model. The weighting is used here to focus on a frequency band of interest. A fixed number of Levenberg-Marquardt iterations is performed. The models obtained after a successful Levenberg-Marquardt iteration (i.e. one for which the cost function evaluated on the estimation data decreases) are retained as candidate models. Models obtained after an unsuccessful iteration are discarded.

4) This last step involves validating the identified nonlinear model on a new data set that was not used in the identification process. This cross-validation step is done to avoid over-fitting. The model among the candidate models (see step 3) that achieves the lowest cost on the validation data is selected as the final model estimate. Here, new swept-sine and broadband data are introduced to measure the performance of the identified nonlinear model.

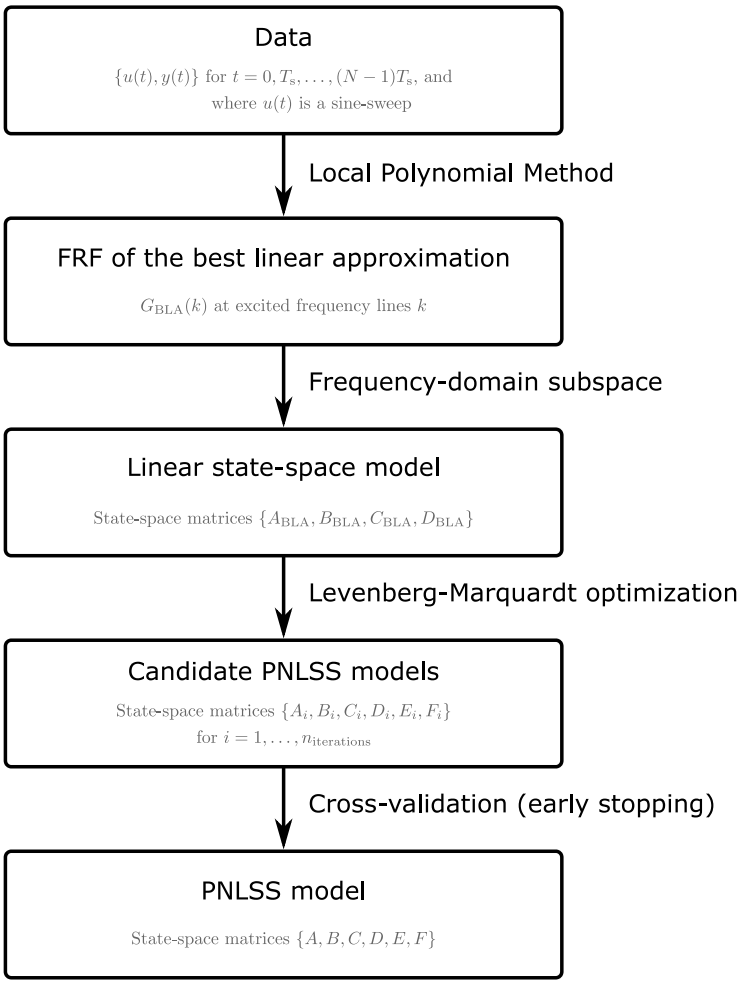

Figure 1: Schematic of the identification procedure

3.1. Non-parametric Analysis of Nonlinear Distortions and parametric BLA

In this section, the Best Linear Approximation (BLA) framework [25, 26] and the Local Polynomial Method (LPM) [22, 27] are employed to gain useful insight into the level of nonlinear distortions

observed in the measured data. These methods are introduced in this section. The estimated BLA is used in the next section as an initialisation for the nonlinear model.

3.1.1. Best Linear Approximation

The BLA of a nonlinear system for a given class of input signals is defined as the linear model $G_{\mathrm{BLA}}(k)$ which produces the best approximation of the system's output in least-square sense [26]:

$$G_{\mathrm{BLA}}(k) = \arg\min_{G(k)} E_u\{\|Y(k) - G(k)U(k)\|_2^2\} \tag{9}$$

where G_{BLA} is the frequency response function (FRF) of the BLA, $E_u\{\cdot\}$ is an ensemble average over the considered class of input signals, $Y(k)$ and $U(k)$ are the discrete Fourier spectra of the output and the input at frequency line k, and G is the FRF of a linear system. The BLA generally varies with the input frequency content and the Root Mean Square (RMS) values of the input signals. It can be identified by performing several experiments and acquiring the steady-state responses of the input-output data. To keep the notation simple, the single input single output case of the BLA estimation procedure is described in this section while a generalisation for multiple input and multiple output nonlinear systems is presented in [28, 29].

Usually, the BLA framework is introduced for Period In Same Period Out (PISPO) systems [26], which means that the response of the system to a periodic input is itself periodic with the same period length, and for (extended) Gaussian input signals [26]. With this condition obeyed, then the BLA of such system exist. The output spectrum of the system can then be written as:

$$Y(k) = G_{\mathrm{BLA}}(k)U(k) + Y_{\mathrm{S}}(k) + V(k) + T(k) \tag{10}$$

where the term $Y_{\mathrm{S}}(k)$ accounts for nonlinear distortions, $V(k)$ accounts for additive measurement noise, and $T(k)$ accounts for leakage due to system and noise transients.

To estimate the BLA and to significantly reduce the effect of leakage, the Local Polynomial Method (LPM) [22, 27] is adopted. The LPM exploits the smoothness over frequencies of $G_{\mathrm{BLA}}(k)$ and $T(k)$, and the roughness over frequencies of $U(k)$, $Y_{\mathrm{S}}(k)$, and $V(k)$. When applying the LPM method the assumption is that the input is random. In that case, the input spectrum is also random, hence does not vary smoothly from one frequency to the other. Similarly, the nonlinear distortions are input dependent (so they are also non-smooth (=rough) over frequency), and V the noise spectrum (so also rough over frequency). The basic idea of the LPM is to model the $G_{\mathrm{BLA}}(k)$ and $T(k)$ as polynomials in a local frequency band around frequency line k:

$$Y(k+r) = G_{\mathrm{BLA}}(k+r)U(k+r) + Y_{\mathrm{S}}(k+r) + V(k+r) + T(k+r) \tag{11}$$

with

$$G_{\mathrm{BLA}}(k+r) = \widehat{G}_{\mathrm{BLA}}(k) + \sum_{s=1}^{R} \alpha_s r^s \tag{12}$$

$$T(k+r) = \widehat{T}(k) + \sum_{s=1}^{R} \beta_s r^s \tag{13}$$

for $r = -n, -n+1, \dots, 0, \dots, n-1, n$ with $n \geq R+1$. With the LPM method, G_{BLA} varies smoothly from one frequency to the other since it is the frequency response function of a linear system that is assumed to have a transfer function with a rational form. $T(k)$ is the transient spectrum and has a rational form (with the same denominator as G_{BLA}).

Putting all unknown coefficients $\widehat{G}_{\mathrm{BLA}}(k), \widehat{T}(k), \alpha_1, \dots, \alpha_R, \beta_1, \dots, \beta_R$ in a parameter vector θ_{LPM}, and rearranging Equations (11) for $r = -n, -n+1, \dots, 0, \dots, n-1, n$ results in a linear regression formulation:

$$Y_n = K_n \theta_{\mathrm{LPM}} + V_n \tag{14}$$

Solving for θ_{LPM} in least squares sense provides an estimate $\hat{G}_{\mathrm{BLA}}(k)$ of the FRF of the BLA. From the residuals, the LPM can also provide an estimate of the covariance matrix of the noise V_n (see for example [22, section 3.1]), which in this case includes the random noise and the nonlinear distortions. The sum of the random noise and the nonlinear distortions are referred to as total distortions later on in the paper.

3.1.2. Parametric BLA

Once a non-parametric FRF model has been estimated, a parametric model is often required to get better understanding of the system's behaviour. To achieve this, a linear state space parametric model with matrices (A, B, C, D) is fitted to the estimated non-parametric $\hat{G}_{\mathrm{BLA}}(k)$ in Equation (12). The fitted linear state space model is attained using the frequency domain subspace identification summarised in [35]. In addition, the quality of the fit for the subspace identification is assessed by introducing a weighted least-squares cost function in the form:

$$V_{\mathrm{L}} = \sum_{k=1}^{f} \epsilon_{\mathrm{L}}^{H}(k) W_{\mathrm{L}}(k) \epsilon_{\mathrm{L}}(k) \tag{15}$$

where f is the number of processed frequencies, superscript H represents the Hermitian transpose while the weighting function is $W_{\mathrm{L}}(k)$, $\epsilon_{\mathrm{L}} = \hat{G}_{\mathrm{BLA}}(k) - G_{\mathrm{L}}(k)$ is the difference between the non-parametric FRF $\hat{G}_{\mathrm{BLA}}(k)$ and the model transfer function $G_{\mathrm{L}}(k)$ that is parameterised in terms of its state-space matrices A, B, C, D. The transfer function of the linear subspace model used to represent the FRF of the parametric BLA is calculated using the expression [30]:

$$G_{\mathrm{L}}(k) = C(z_k\, I_n - A)^{-1} B + D \tag{16}$$

where $z_k = e^{j\frac{2\pi k}{N}}$ represents the Z-transform variable, $I_n \in \mathbb{R}^{n \times n}$ is an identity matrix with n being the most suitable model order required to achieve the lowest fitting error from the cost function minimisation. Further minimising the cost function with respect to all the linear state space parameters in (A, B, C, D) with a Levenberg-Marquardt optimisation method often improves the quality of the fitting results obtained for the linear model. The total number of linear parameters is equal to the number of elements in the matrices (A, B, C, D) which is equal to $(n_a + n_u)(n_a + n_y)$. In addition, physical interpretation can also be obtained from optimised model of (A, B, C, D) based on a transformation of the discrete-time model result to a continuous-time model. This can be achieved under the assumption of a zero-order hold inter-sample behaviour of the input signal. Under this assumption, the relationship between the state-space matrices (A, B, C, D) of the discrete-time model and the state-space matrices ($A_{\mathrm{CT}}, B_{\mathrm{CT}}, C_{\mathrm{CT}}, D_{\mathrm{CT}}$) of the continuous-time model is summarised in [30]. The natural frequencies and damping ratios of the optimised model are computed from the poles of the continuous-time model, where the poles are the eigenvalues of A_{CT}. In particular, the natural frequencies are the imaginary parts of the poles. The damping ratios can be calculated by dividing the absolute value of the real parts of the poles by the modulus of the poles.

3.2. Initialisation of the nonlinear model

The parameters of the PNLSS model are the elements in the matrices A, B, C, D, E, and F, and the initial conditions $x(0)$ and $u(0)$. They are stacked up in a vectorised format as

$$\theta_{\mathrm{NL}} = \left[\mathrm{vec}(A); \mathrm{vec}(B); \mathrm{vec}(C); \mathrm{vec}(D); \mathrm{vec}(E); \mathrm{vec}(F); \mathrm{vec}\big(x(0)\big); \mathrm{vec}\big(u(0)\big)\right] \tag{17}$$

and estimated by minimizing the difference between the measured output y_{measured} and the modelled output y_{model} in (weighted) mean-square sense. That is, the cost function (19) is minimized.

Since the modelled output is nonlinear in its parameters, the minimization problem is a nonlinear optimization problem that requires a good initial estimate of the parameters. The best linear approximation method, as described in Sections 3.1.1 and 3.1.2, will be used to initialise the full nonlinear model. The matrices A, B, C, and D are initialised with the matrices of the linear model obtained in section 3.1.2. The other parameters are initialised as zeros.

3.3. Identification of the full PNLSS model based on optimisation

To improve the results obtained based on the BLA initialisation, a full nonlinear model is required to identify the final nonlinear state-space parameters (*A*, *B*, *C*, *D*, *E*, and *F*). This step involves identifying the appropriate nonlinear terms and parameters in matrices E and F that would capture the nonlinear dynamics in the measured data. In this case the matrices E and F are intialised as zero value matrices of the appropriate dimension. The full nonlinear model is then parameterized by a parameter vector θ_{NL}, where:

$$\theta_{\mathrm{NL}} = \left[\mathrm{vec}(A); \mathrm{vec}(B); \mathrm{vec}(C); \mathrm{vec}(D); \mathrm{vec}(E); \mathrm{vec}(F); \mathrm{vec}\big(x(0)\big); \mathrm{vec}\big(u(0)\big)\right] \tag{18}$$

An estimate of these parameters is found by minimizing the second weighted least-squares cost function

$$V_{\mathrm{WLS}}(\theta_{\mathrm{NL}}) = \sum_{k=1}^{N_F} E^H(k, \theta_{\mathrm{NL}}) W(k) E(k, \theta_{\mathrm{NL}}) \tag{19}$$

with respect to θ_{NL}. Here $W(k)$ is a user chosen frequency domain weighting matrix. It is selected to put more weight in a frequency bandwidth of interest or bandwidth where nonlinearities are assumed to be more evident. The accuracy of the final optimised nonlinear model is evaluated based on the model error which is given by:

$$E(k, \theta_{\mathrm{NL}}) = Y_{\mathrm{model}}(k, \theta_{\mathrm{NL}}) - Y_{\mathrm{measured}}(k) \tag{20}$$

where $Y_{\mathrm{model}}(k, \theta_{\mathrm{NL}})$ and $Y_{\mathrm{measured}}(k)$ are the Discrete Fourier Transform (DFT) spectra of the modelled and the measured output (the modelled output $y_{\mathrm{model}}(t)$ is denoted $y(t)$ in (4)). It is worth noting that the variables such as E and Y are expressed in uppercase letters to distinguish the frequency domain error computation from the time domain errors which are in expressed in lower case. The final optimised parameters are obtained as the minimising argument of the cost function $V_{\mathrm{WLS}}(\theta_{\mathrm{NL}})$

$$\hat{\theta}_{\mathrm{NL}} = \arg\min_{\theta_{\mathrm{NL}}} V_{\mathrm{WLS}}\,(\theta_{\mathrm{NL}}) \tag{21}$$

This unconstrained optimisation is performed using the Levenberg-Marquardt (LM) algorithm [24, 26]. Minimizing the cost function corresponds to solving a nonlinear minimisation problem and can be sensitive to the starting values, especially when using a gradient based algorithm such as LM.

The LM algorithm is an iterative algorithm that can be seen as a mixture of the gradient-descent and the Gauss-Newton algorithm where the trade-off is determined by the Levenberg-Marquardt parameter λ. The limiting cases λ = +∞ and λ = 0 correspond to gradient-descent with a zero step-size (the step-size decreases for increasing values of λ) and Gauss-Newton, respectively. Close to a local minimum, the Gauss-Newton method can converge faster, but there is no guarantee of convergence if the current parameter guess is far away from a local minimum. In contrast, the gradient-descent method is more robust where under some conditions, it is guaranteed to converge to a local minimum of the cost function, but convergence in the vicinity of a local minimum can be slow. Technicalities and further discussions related to this optimisation algorithm are elaborated in [24] and [31].

To avoid the optimisation getting stuck in a local minimum, appropriate starting parameters are required. A systematic way to get an initial parameter is to start from the initial values obtained from the Best Linear Approximation. This does not always guarantee that the optimisation will find a global minimum, however this strategy has been adopted for different applications and examples with succesful results as demonstrated in [14,15,19]. In addition, starting from the Best Linear Approximation guarantees that the result of the optimised nonlinear model cannot be worse than the best linear model on the estimation data.

4. Description of the Test Structure

The study presented in this paper was performed on an aero-engine casing assembly structure presented in Figure 2. This type of aircraft engine casing assembly is often used for powering a typical commercial aircraft. The structural configuration of the casing assembly considered in this paper is a three-layer architecture without any internally attached accessories such as blades, shafts and other rotating components. The aero-engine casing assembly is made of three components comprising of casing A, casing B, and casing C as shown in Figure 2. The entire assembled casing has structural features that are typical of a full-size assembled system e.g. multiple body sections and bolted joints. The total mass of this casing assembly is 461kg.

The first cylindrical section of the casing (Casing A) has an aluminium plate with four low stiffness shaped steel blocks mounted on it as shown in Figure 2. As demonstrated in [32], the mounted plate forms an additional source of non-linear behaviour in the entire casing assembly. It introduces localised nonlinearities from the bolted joints and large deformation of the plate depending on the mode of interest and also reflects on typical operational measurement limitations. To study the nonlinear phenomena exhibited by the entire assembly in a rather simplified approach, only the first cylindrical section of the casing (Casing A) was instrumented to obtain measured data during the experimental campaign as shown in experimental set-up in Figure 4a.

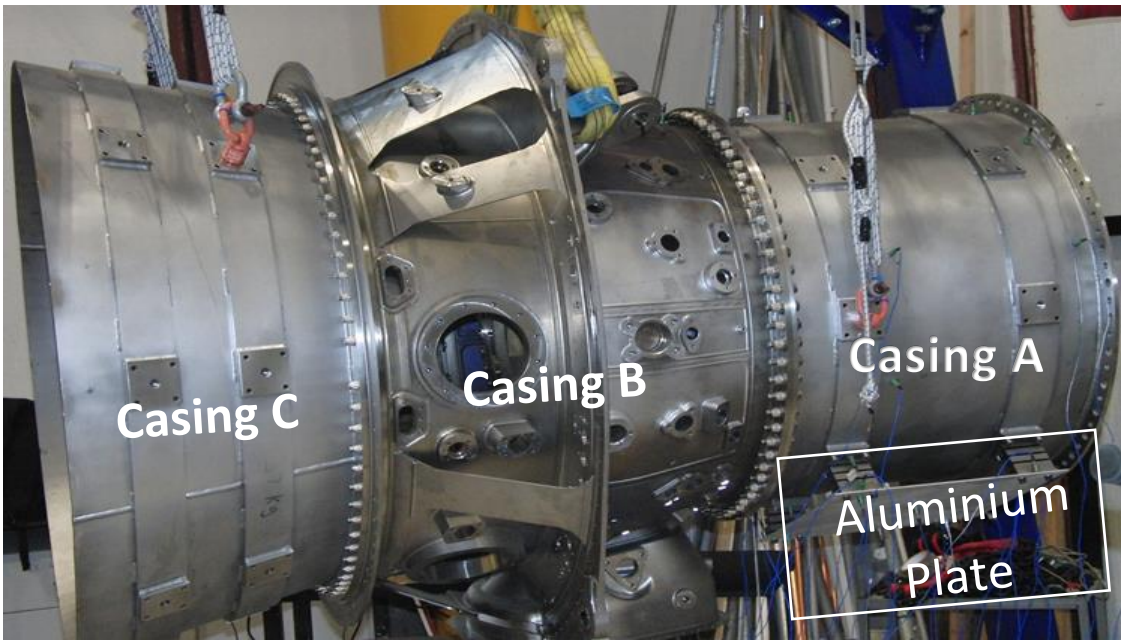

Figure 2: Aero-engine casing and the attached aluminium plate in the bottom right corner

4.1. Linear Finite Element Modal Analysis

Pre-test analysis is a vital step of experimental modal testing and analysis, it often has direct effect on the accuracy and results of test and analysis. A detailed Finite Element (FE) model of the casing assembly was developed using the commercial ABAQUS FE package, all parts of the casing and the plates were modelled using shell elements. The bolts and joints were modelled with tie constraints and fasteners with specific spring coefficients. A linear FE modal analysis was conducted to extract the FE mode shapes. The linear FE analysis was conducted with the aim of getting better insight into the selection of appropriate measurement locations, sensor placement and the test excitation point. In addition, the initial FE analysis was used to determine the number of expected modes in a given frequency range. Most importantly, since the test was being conducted on a large aerospace structure with multiple joints and localised nonlinearities, the results from the FE mode shapes were used to quickly and reliably identify the frequency ranges where the joints and additional localised nonlinear source were actively excited. The FE analysis highlighted 20 mode shapes between 0-350 Hz. A complete summary of the FE modal analysis is not included in this paper. However, it is sufficient to state that the modes of vibration that engaged the entire casing assembly and the plate were calculated to have FE natural frequencies of 83.95 Hz and 87.12 Hz as shown in Figure 3a and 3b.

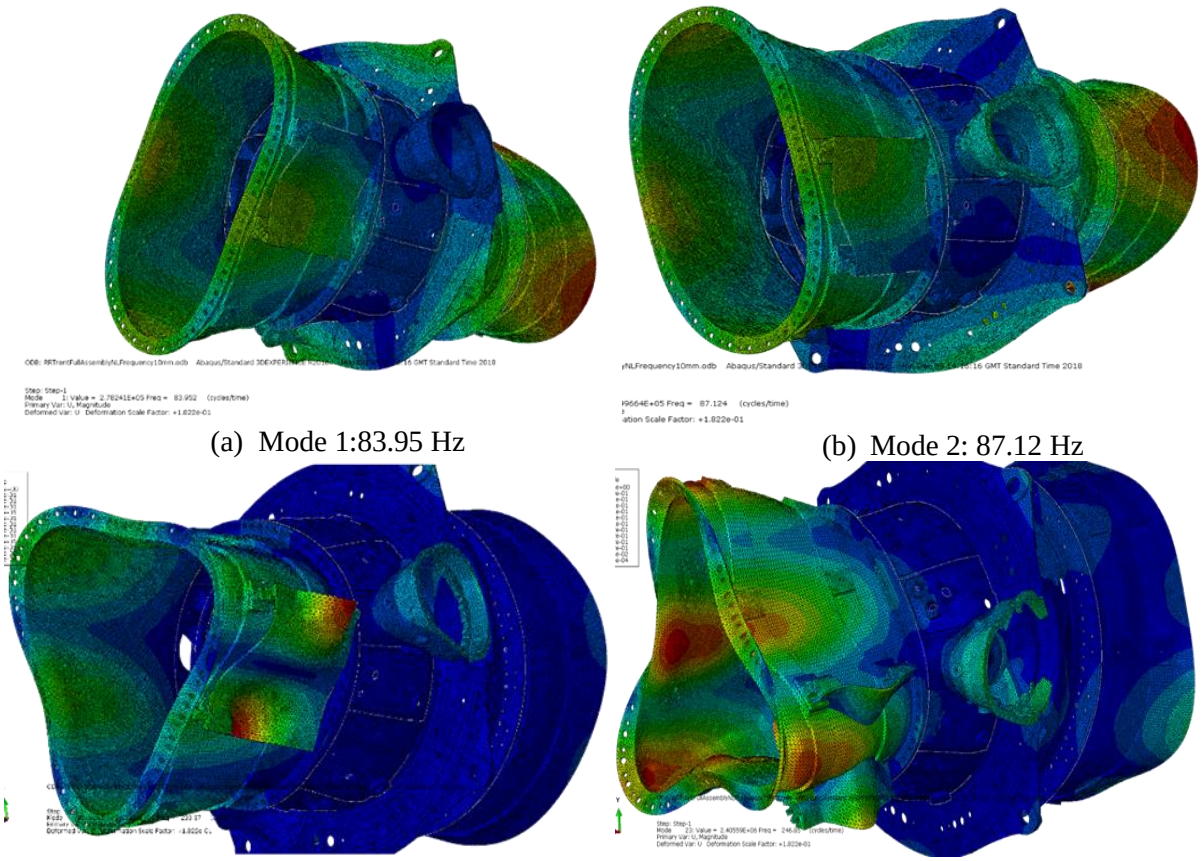

(a) Mode 1:83.95 Hz (b) Mode 2: 87.12 Hz

(c) Mode11: 233.27 Hz (d) Mode 14: 246.85 Hz

Figure 3: Selected mode shapes obtained from the 3D FE modal analysis

In addition, an area of interest on the casing assembly is the bolted connection between casing A and the aluminium plate. One of the main reasons for this interest is to understand the influence of connected devices on the casing and their potential introduction of local and geometrical nonlinearities to entire structure. The FE model was also able to highlight the modes of vibration of casing A and plate with natural frequencies ranging between 180 to 300 Hz. Of all modes of vibration highlighted by the FE model, only those that are prone to stimulate all joints and plate connections are further investigated in

the nonlinear identification section of this paper. Figure 3c and 3d illustrate a selection of modes of vibration where the joints and local nonlinear sources are stimulated.

4.2. Experimental Setup and Linear Modal Analysis

The casing was suspended horizontally from a test frame using four elastic chords as shown in Figure 4a. The test frame used in this research is classified as a Technology Research Level (TRL6) structure developed under the Highly Innovative Technology Enablers for Aerospace (HiTEA) project while the elastic chords are used to represent a free-free boundary test condition. The experimental set-up was designed to replicate the traditional horizontal configuration of such component when attached to an aircraft. A total of 32 Integrated Circuit Piezoelectric (ICP) type single-axis acceleration sensors were employed to instrument the structure. For this investigation, only the first subassembly section casing A where the plate is bolted to the engine casing, as illustrated in Figure 4b, was fully instrumented. A large shaker visible in Figure 4a was used to apply the excitation inputs to the casing in a vertical direction.

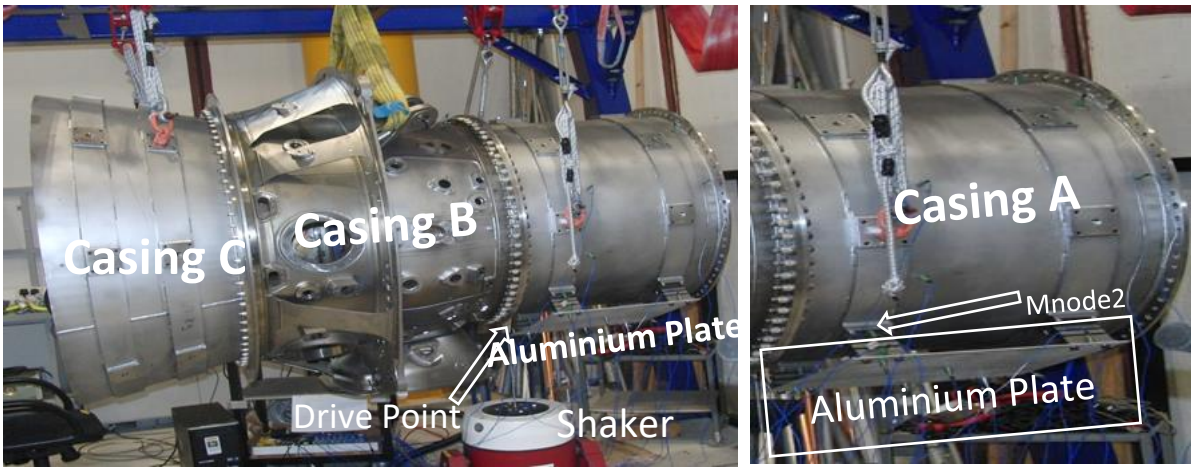

a *b*

Figure 4: Experimental set-up of the engine casing suspended on a TRL-6 frame: (a) Test set-up, (b) Instrumented section of the casing.

The first stage of the experimental investigation involved conducting a set of traditional modal tests on the casing and plate assembly to obtain the natural frequencies and damping ratios at low amplitude of vibration. In addition, a force controlled stepped-sine test at high excitation levels was carried out on the assembly to check for the symptoms of nonlinearity that could be present in the instrumented section of the casing. A preliminary experimental study highlighting nonlinearities observed at the high amplitude of vibration was already conducted on the engine casing assembly in [32]. There, the linear FE mode shapes were used to gain an insight into the regions of the assembly that could potentially show some form of nonlinear behaviour. The first measurements obtained from the test comprised of several low-amplitude responses which were acquired based on the broadband random excitation. The choice of the broadband excitation was made based on its conventional use in modal testing. The low level random excitation test was performed using the Spectral Test module in LMS Test Lab. The test structure was excited near the flange connecting the casing B with casing A as shown in Figure 4a. The structure was excited using burst random excitation ranging between 30 and 320Hz and the applied random excitation had an RMS value of 45N. The Frequency Response Functions (FRFs) obtained from the test were used to identify the linear modal parameters of the entire assembly. Figure 5 shows a selection of the FRFs obtained from the low-level test.

A linear modal analysis based on the FRFs obtained from the low-level random test was conducted using the PolyMAX method [33]. Table 1 presents the corresponding natural frequencies and damping ratios of the casing A with the aluminium plate bolted to it.

Table 1: Estimated natural frequencies and damping ratios based on the low-level excitation

Mode Number	Natural Frequency (Hz)	Damping Ratio (%)	Mode Number	Natural Frequency (Hz)	Damping Ratio (%)
1	82.17	0.29	9	179.68	0.19
2	84.34	0.19	10	237.51	0.34
3	87.17	0.09	11	238.68	0.12
4	158.42	0.13	12	243.45	0.28
5	163.41	0.39	13	247.01	0.39
6	167.29	0.57	14	285.51	0.42
7	169.98	0.46	15	287.72	0.37
8	172.05	0.46	16	312.51	0.29

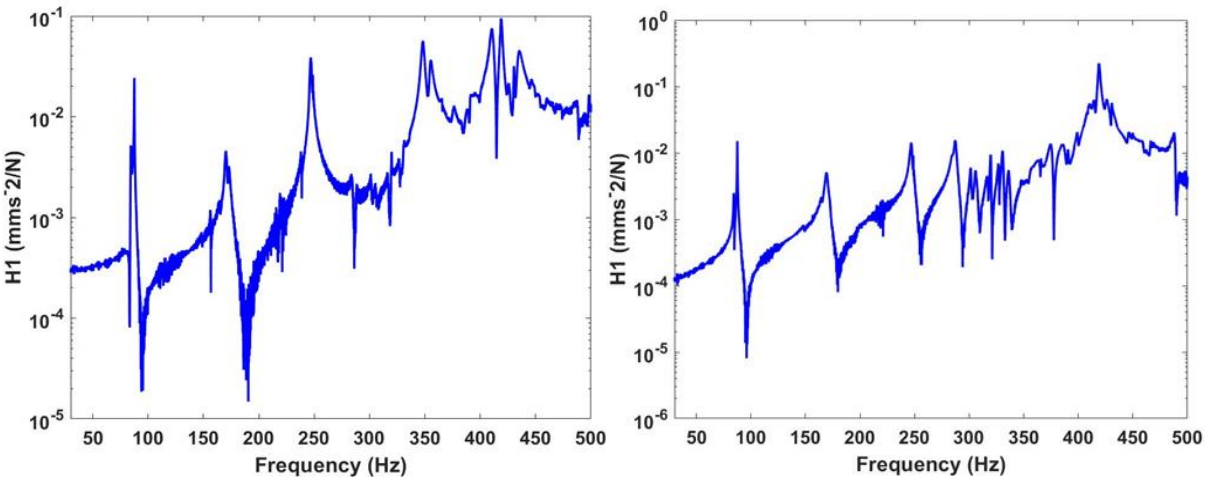

(a) *(b)*

Figure 5: Acceleration FRFs obtained from the low-level broadband excitation test (a) Mnode2 FRF (b) Drive point FRF.

4.2.1. Non-Linear Detection Based on Distortions of Measured Data

To check for the symptoms of nonlinear behaviour in the casing and plate assembly, several tests were conducted on the entire assembly using two different types of excitation signals. In this paper, stepped and swept-sine excitation signals were used for investigating the nonlinear effects observed in the measured responses of the assembly from low to higher excitation levels. Stepped and swept sine signals were selected based on their deterministic nature. For a linear system or structure, the output response would produce a pure sine wave and for a nonlinear case, distortions are easily detected by visualising the output response to the sine wave input. In Figure 6, the stepped-sine FRFs are presented for the test concentrated around the vibration modes that proved to stimulate the connections between the plate and casing A as illustrated in Figure 3. Input excitation force was ranged from the lowest (10N) to the highest level (100N) and a frequency resolution of 0.1Hz was selected for the measured FRFs. These stepped-sine FRFs only consider the first harmonic and neglect all other higher-order harmonic components in both input and output [34]. Figure 6 shows the lack of homogeneity in the measured FRFs over different excitation levels, indicating thus a clear breakdown of the superposition principle. Evidence of nonlinearity is observed based on the shift in the maximum amplitude and its corresponding frequency for the measured frequency bandwidth of 230-241Hz and 282-296Hz. In addition to the observed frequency and amplitude shifts, the resonant peaks also lean to the left as shown in Figure 6 a and b, causing a sudden transition (jump) down to a lower energy state when decreasing the excitation frequency. This is most evident in the FRFs illustrated in Figure 6a and b for the frequency bandwidth of 237-241Hz.

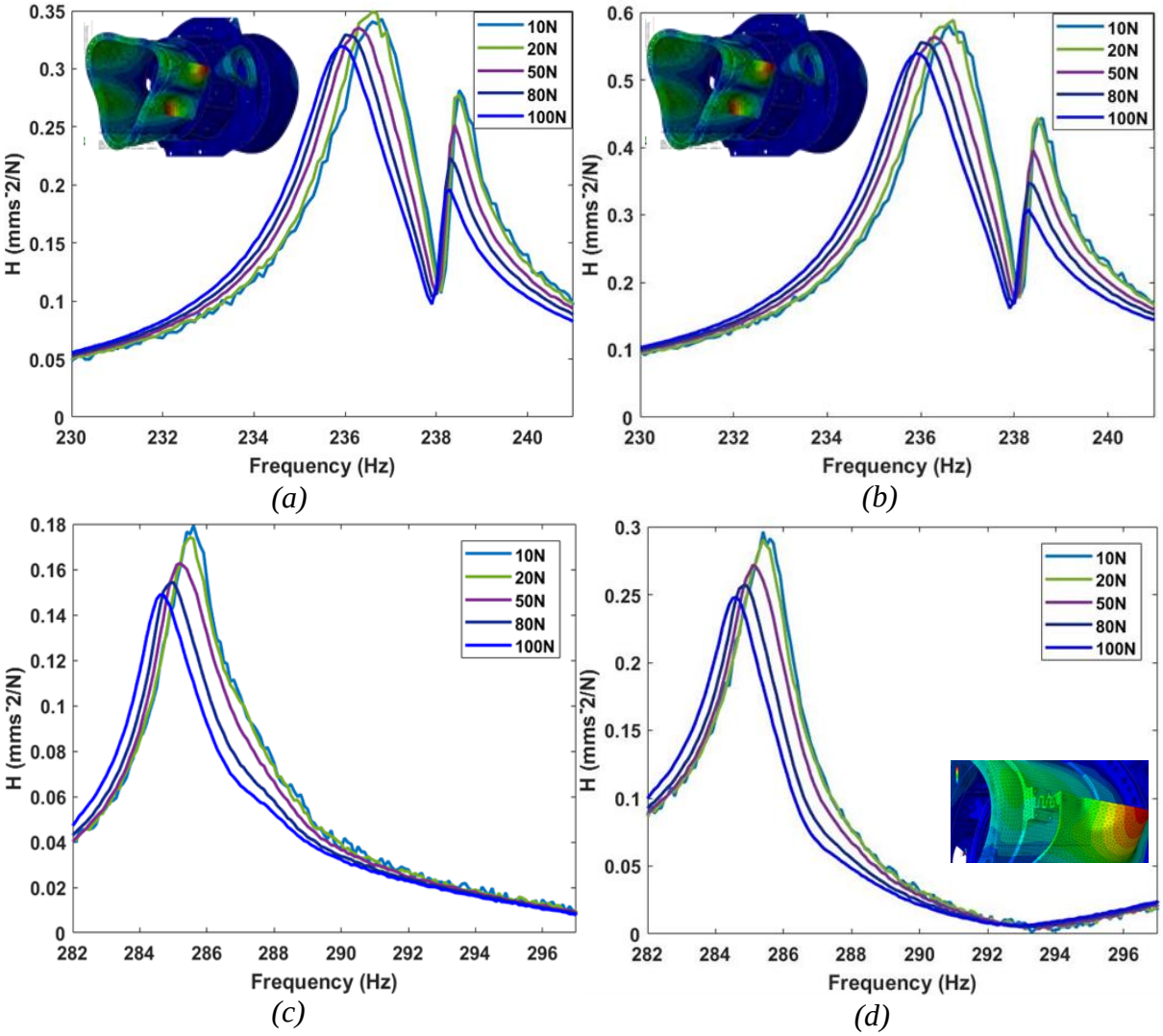

Figure 6: Force controlled stepped sine acceleration response: (a) Mnode 2 FRF for frequency range 230-242Hz, (b) Drive point FRF for frequency range 230-242Hz (c) Mnode 2 FRF for frequency range 282-296Hz (d) Drive point FRF for frequency range 282-296Hz.

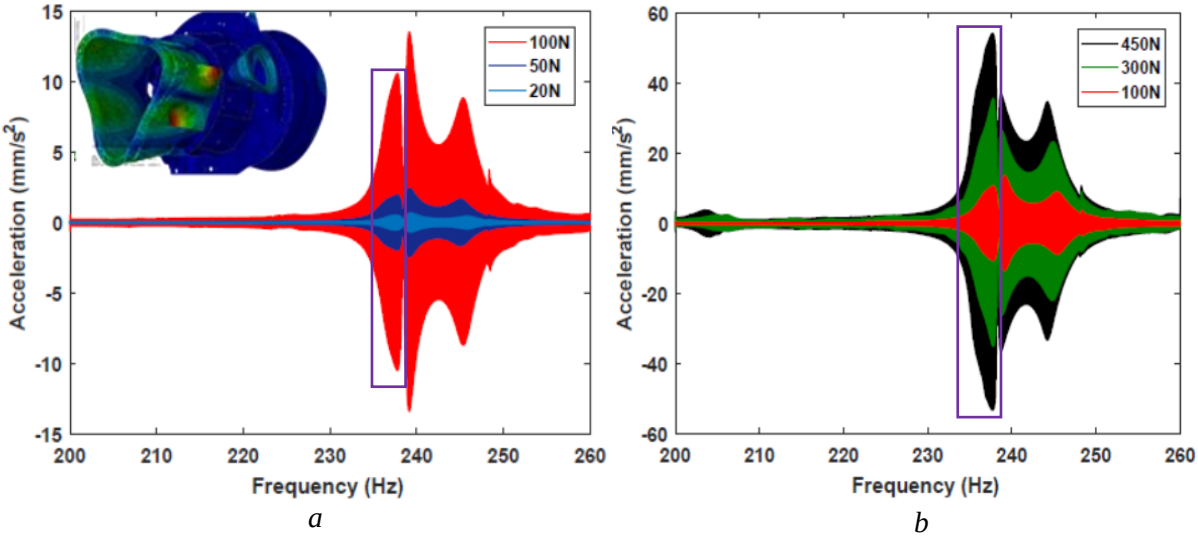

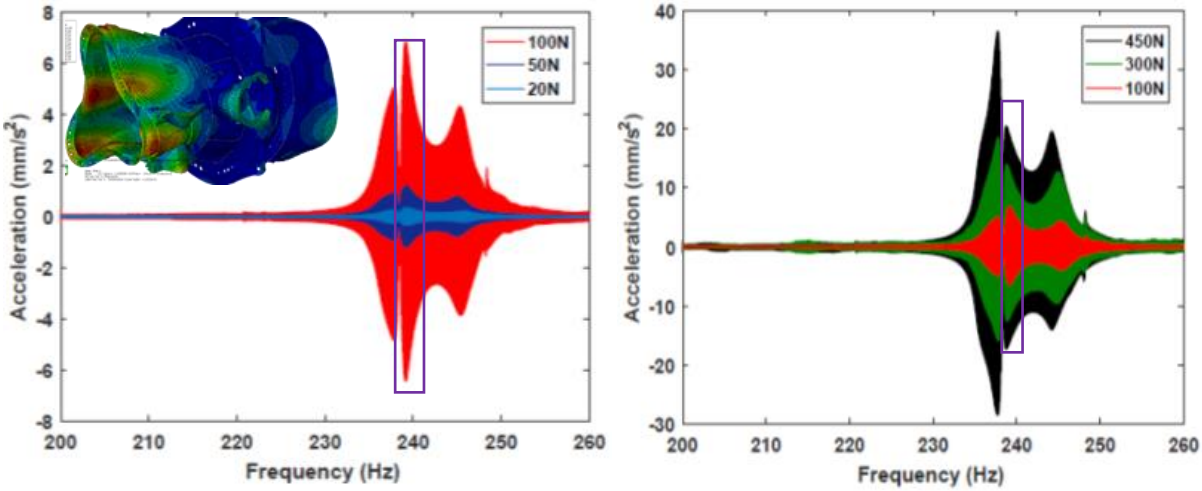

c *d*

Figure 7: Sine-sweep acceleration responses measured on two different locations of the assembly. a and b (Drive point) b and d (Mnode2).

Sine-sweep test was also conducted on the casing assembly at multiple excitation levels to gain some insight into the time series data. The sine-sweep test was conducted to cover a frequency bandwidth of 200-260 Hz. Accelerations at two selected locations of the assembly shown in Figure 4 were measured at 20N, 50N, 100N, 300N and 450N RMS excitation levels. Figure 7 shows selected plots of the measured acceleration against the sweeping frequency for the modes of the assembly in that bandwidth. Symptoms of nonlinearity are visible in the plots presented in Figure 6 where a frequency shift is observed for all modes when the amplitude of vibration is increased. The lack of symmetry feature is also observed around the resonance peak of 238Hz for high amplitude of vibration, this is more obvious in Figure 7b and 7d. Skewness of the signal envelope is also observed around the resonance peaks at high excitation level resulting from a jump phenomenon. In practice, many nonlinearities exhibit a degree of amplitude dependence and most of these become more prominent at higher levels of vibration rather than low levels. In this case of the aero-casing assembly, nonlinear behaviour is clearly observed at higher excitation amplitude using a variety of excitation signals. Therefore, it is important to conduct further analysis on the casing assembly to explore the type of nonlinearities detected from the measured data.

4.3. BLA estimation of the casing assembly

To calculate the BLA of the measured data for the casing assembly, sine-sweep input and output data acquired during the nonlinear detection phase were used for the calculation. The sine-sweep data were focused around frequency bands of 70-93Hz and 200-260Hz. These frequency bands were chosen based on the linear FE mode shapes illustrated in Figure 3 where the joints and connections between casing A and the plate are activated. The aim of the BLA estimation is to explore the evolution of the nonlinear distortions observed in the measured sine-sweep data across a range force excitation levels. Although a sine-sweep is a deterministic signal instead of a random one, the initial linear state space and the FRF of the BLA can still be obtained using the expression given by:

$$G_{\mathrm{BLA}}(k) = \frac{Y(k)}{U(k)} \tag{22}$$

at the excited frequency lines k. The fact that the spectrum $U(k)$ of a sine-sweep is not rough at all frequencies could pose a challenge in the calculation [27], however the LPM can still be applied based on calculating the difference between the input at two consecutive frequencies i.e., $(U(k) - U(k-1))$. The specific assumption made in [27, section 2.3] is that $U(k) - U(k-1)$ should not vanish to zero (it should remain in the same order of magnitude as $|U(k-1)|$ with probability 1). The intuition behind

$U(k) - U(k-1)$ characterizing the smoothness of the input spectrum is as follows. If the input spectrum is constant over frequency (globally or in a local frequency band), it is extremely smooth, and $U(k) - U(k-1)$ vanishes to zero. On the other hand, if the input spectrum is rough over frequency (i.e. it varies a lot), then the difference $U(k) - U(k-1)$ does not vanish to zero (relative to $U(k)$). The results obtained from the difference in spectrum calculation are presented in Figure 8 for frequency bandwidth of interest. As shown in Figure 8, the spectrum $(U(k) - U(k-1))$ remains the same or at least within the same order of magnitude as $U(k)$ in a large part of the frequency band of interest and only approaches to zero at 70Hz and 93Hz for Figure 8a and 200 Hz and 260 Hz for Figure 8b. This means that the spectrum $U(k)$ is sufficiently rough in the frequency band of interest. Therefore, this indicates that the LPM will be able to locally smooth the FRF for the BLA estimation.

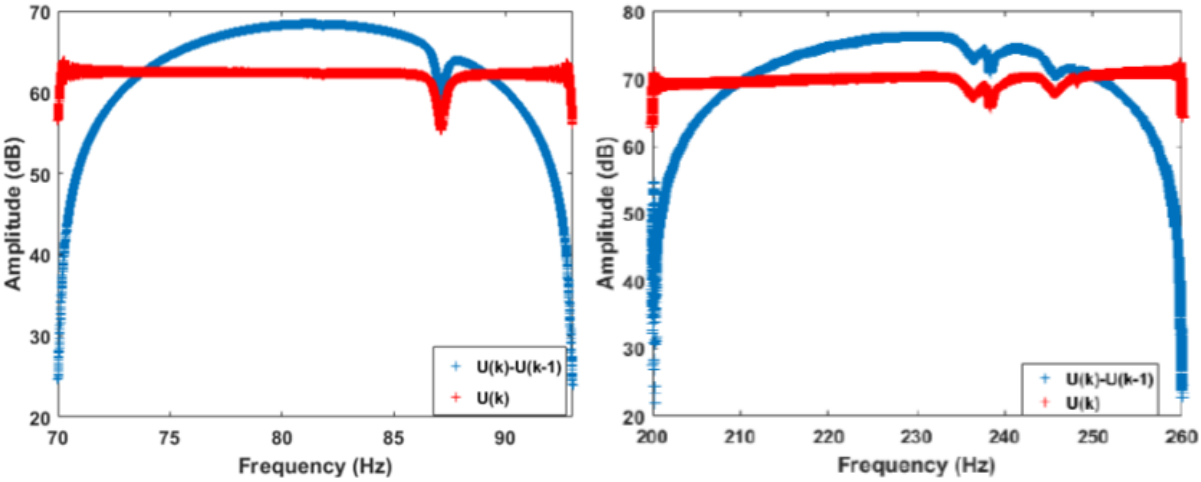

(a) *(b)*

Figure 8: The difference of the sine sweep input spectrum (U(k)-U(k-1)) of the interested bandwidth. (a) Frequency range 70-93Hz, (b) frequency range 200-260Hz,

Figure 9 shows the estimated FRFs and amplitude of total distortions for the non-parametric BLA for two main frequency bandwidths of interest 70-93Hz and 200-260Hz. The selected FRFs and total distortion (which include noise and nonlinear) levels are based on excitation levels ranging from 20N to 100N. The noise and nonlinear distortion levels across the input band mostly lie below -20dB. Slight shift in the resonance peaks and reduction in amplitude is observed across the FRFs obtained from the multiple forcing level BLA estimations when the excitation level increases. Similarly, it is evident that the total distortion also affects the response of the structure. One can observe that the level of total distortions increases as the forcing changes from 20N (blue) to 100N (red) for each frequency bandwidth of interest. The increase in total distortion response at higher excitation levels in this figure is a clear indication of the presence of nonlinearities in the measured sine-sweep data. Therefore, linear approach can no longer be used to produce a sufficiently accurate representation of the characteristics observed in the measured data.

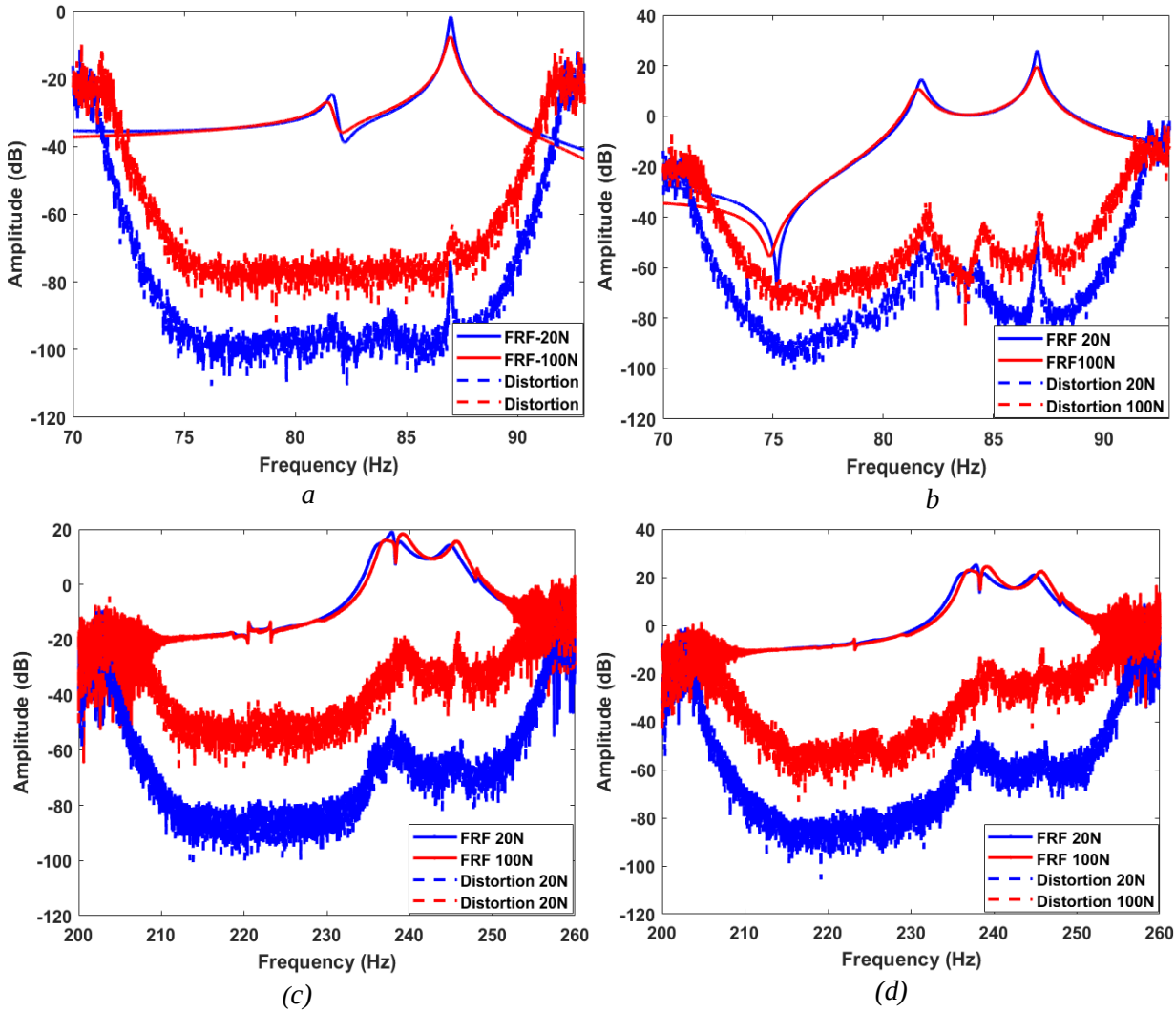

Figure 9: Non-parametric FRFs and total distortions: a (Mnode 2 for 70-93Hz) b (Drive point for 70-93Hz) c(Mnode2 for 200-260Hz) d (Drive point for 200-260Hz).

4.3.1. Linear State Space Model

Before developing a PNLSS model, a linear state space model of the system under consideration is required. In this paper, the linear state space model for the casing assembly is identified from the previously estimated BLA using the frequency domain subspace method described in [23, 35]. The accuracy of the fitted state space model is evaluated using a similar weighted least squares cost function expressed in Equation (15). In this case, the inverse of the estimated total variance of $G_{BLA}(k)$ is chosen as a weighting function.

$$V_{\mathrm{L}} = \sum_{k=1}^{F} \frac{\left|G_{\mathrm{BLA}}(k) - \hat{G}_{\mathrm{BLA}}(k)\right|^2}{\sigma_{\mathrm{BLA}}^2(k)} \tag{23}$$

where $\sigma_{\mathrm{BLA}}^2(k)$ represents the total distortions observed in the model. The model fitting error is then calculated based on the difference between the parametric and non-parametric BLA:

$$\epsilon_{\mathrm{L}} = G_{\mathrm{L}}(k) - G_{\mathrm{BLA}}(k) \tag{24}$$

The parametric and non-parametric BLA models were estimated for different excitation levels ranging from an RMS value of 20N to 100N (see Figure 9). A sufficiently accurate fit is observed between the parametric and non-parametric estimation of the BLA based on a selected model order of 6. Discrepancies are only noticed at the start and end frequencies of the bandwidth of interest.

A time domain least squares cost function which calculates the squared error between the simulated model outputs and the measured data was implemented to evaluate the accuracy of the linear state space model. The cost function expressed in Equation (23) is introduced to assess the quality of the fit for the linear subspace identification. Figure 10 depicts the comparison between the simulated results obtained from the linear state space identification and the measured data.

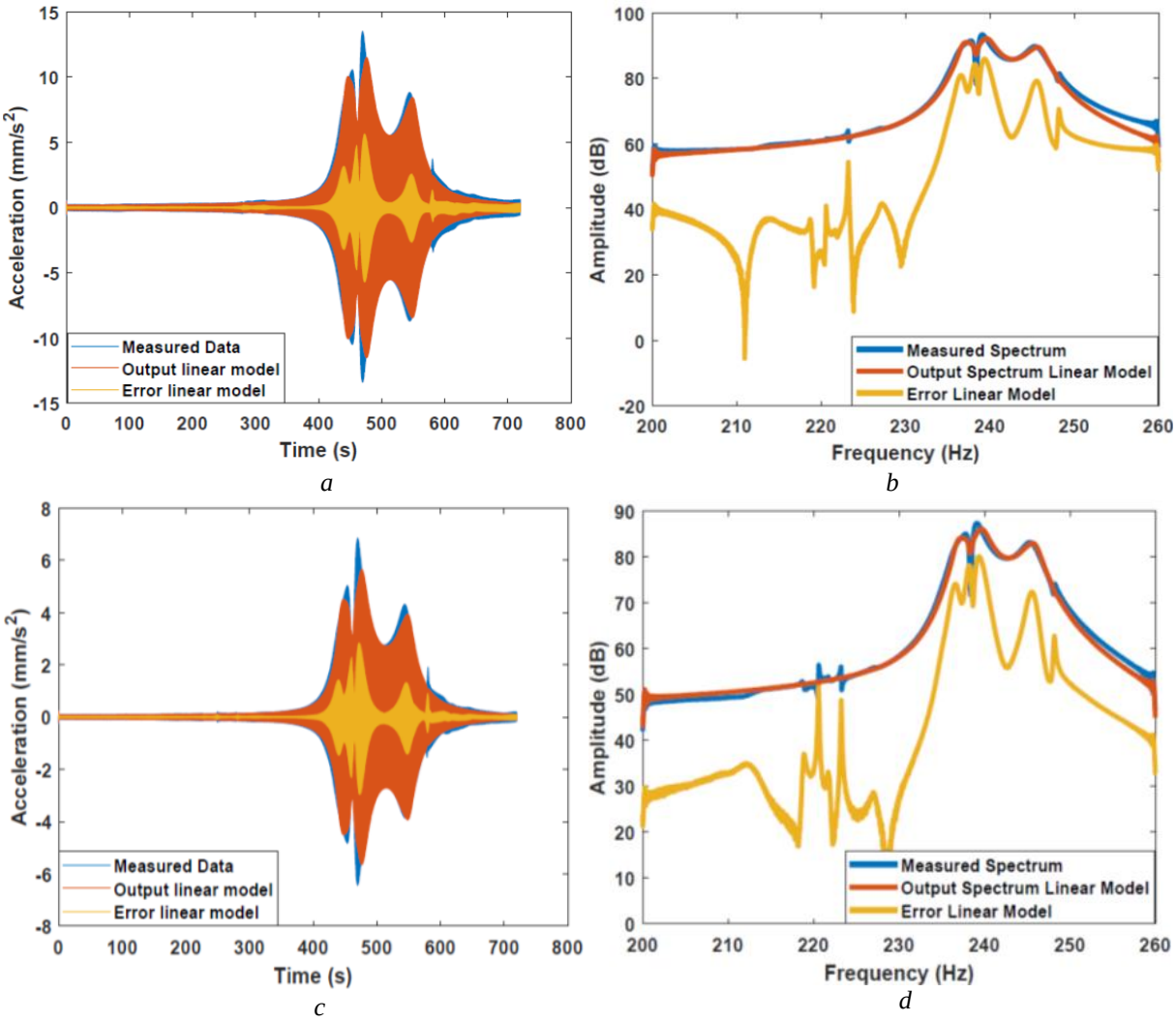

Figure 10: Comparison of initial linear model against measured data: a (time domain for drive point), b (frequency domain for drive point), c (time domain for Mnode), d (frequency domain for Mnode).

Judging from the time and frequency domain results presented in Figure 10, the results show that the initial identified linear model has a reasonable agreement with the measured data. However large errors and discrepancies are observed mainly around the resonance regions which show a clear indication that the nonlinear dynamics are not yet captured. The acceleration values at the resonance region are larger and, in this case, may mean that the nonlinearities are stronger in those sections of the measured data. It is therefore evident that the nonlinear behaviour cannot be captured by a linear model and as such a full identification is required to accurately capture the nonlinear dynamics in the measured data. The normalized Root Mean Squared (RMS) error of the linear model on the estimation dataset was 52.6%. Such a relatively high RMS percentage value is also an indication that the proposed linear model is not sufficient and thus requires further identification and minimisation of the selected cost function.

4.4. Nonlinear Identification of the Casing Assembly

This section focuses on developing a data driven nonlinear model to represent the nonlinearities observed in the aero-engine casing assembly based on PNLSS model. Here, the sine-sweep excitation at 100N RMS is used as the estimation data set, while the nonlinear identification is focused around the frequency bandwidth of 200-260 Hz. Furthermore, a study on using different monomial combination shown in Table 2 for the polynomial degrees selection such as consecutive, non-consecutive, even, and odd was conducted.

Table 2: Overview of the polynomial order implemented in the PNLSS identification

PNLSS Model study	Polynomial Degrees
1	2-3
2	2-3-4-5
3	2-3-4-5-6-7
4	2-4
5	2-4-6
6	3-5
7	3-5-7

4.4.1. Full Nonlinear Model

To begin this stage, the linear state space model characterised by the matrices A, B, C, and D estimated in the previous section was used as an initial starting value while the elements of the matrices E and F in Equation (18) are initialized as zero. The PNLSS model is evaluated by defining the weighted least-squares cost function $V_{\mathrm{WLS}}(\theta_{\mathrm{NL}})$ expressed in Equation (19). The final estimates of the nonlinear state space parameters (A, B, C, D, E, F) are obtained by minimising the cost function $V_{\mathrm{WLS}}(\theta_{\mathrm{NL}})$. Here, the parameters in the matrices E and F that correspond to a term in which the input is raised to a non-zero power, is not optimized, but kept at its initial zero value. In other words, polynomial terms in the states only are considered. A unit weighting $W(k)$ is applied as shown in Equation (19) for focusing on the frequency band 200-260 Hz during the minimisation of the weighted least-squares cost function in the frequency domain. Unit weights are chosen in the frequency band of interest, while weights of 0.05 are chosen outside this band. It is important to give a non-zero weight to the data outside the frequency band of interest, since not using the information at those frequencies would lead to an ill-conditioned optimization problem (with more unknown parameters than data samples used). The cost function is minimised with the Levenberg-Marquardt algorithm.

In this research, the Levenberg-Marquardt method is initialised with $\lambda = 200$. This relatively large number is selected to make the optimisation process more robust. When an iteration is successful, (i.e. the cost function decreased on the estimation data), the Levenberg-Marquardt parameter λ is adjusted to half of its previous value in order to make the optimisation algorithm to lean more towards the Gauss-Newton method. This approach further improves the speed of the iterative process. In the case of an unsuccessful iteration, the Levenberg-Marquardt parameter λ is multiplied with a factor $\sqrt{10}$ to lean the method more towards a gradient-descent algorithm with a decreased step-size for further optimisation improvement and increased robustness. For all simulated PNLSS cases in this paper, a fixed number of 150 iterations of the Levenberg-Marquardt method was selected. This number signifies a trade-off between the convergence and computational time. The sine sweep data obtained at the 100N level of excitation were used for the PNLSS model estimation. The estimated PNLSS model was developed using a state only model structure with a model order of 6 while polynomial degrees of the order 2, 3, 4, 5, 6, and 7 were used for this PNLSS estimation. The results obtained from running the optimisation problem are presented in Figure 11.

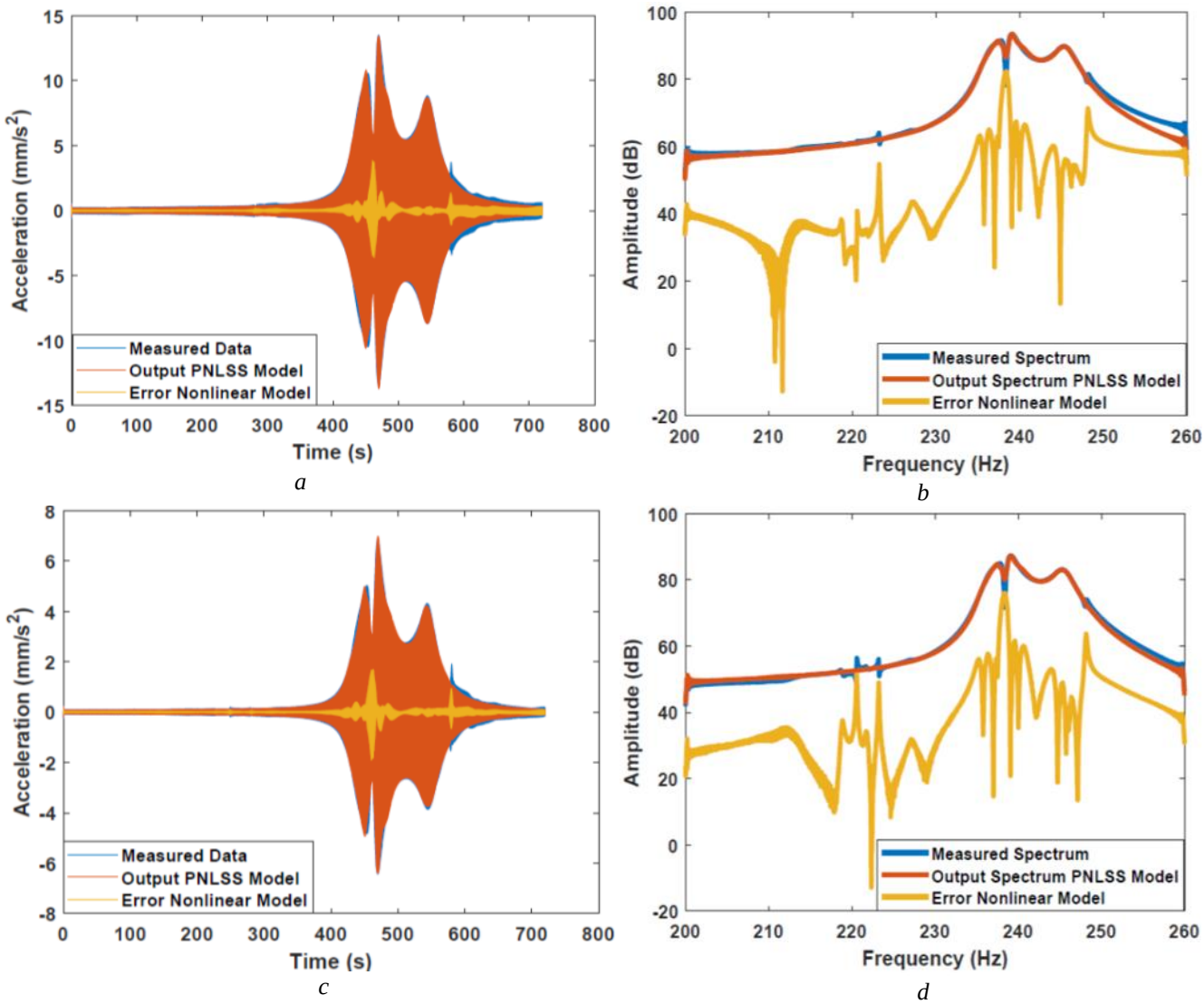

Figure 11: Comparison of the identified PNLSS model against measured data: a (time domain for drive point), b (frequency domain for drive point), c (time domain for Mnode), d (frequency domain for Mnode).

Comparing the full PNLSS results with the initially estimated results in Figure 10, one can observe a significant improvement in the PNLSS model compared to the initial linear model. The optimised PNLSS model improves on the results of the initial linear model, in particular around the resonant frequencies as shown in Figure 11. This is a clear indication that the PNLSS model has successfully been able to capture a large portion of the nonlinear responses that were not captured in the initial linear model presented in Figure 10. A significant improvement was also observed in the RMS percentage value after running the optimisation. Compared to the initial estimated model, a much lower time domain RMS value of 7.2% was obtained for the PNLSS model. This shows a significant reduction of about 45% in the RMS error between the identified linear state space model and the final estimated PNLSS model. A subsequent validation of the identified PNLSS model on a new set of sine sweep data yields a comparably small time domain RMS error of 9.1%. With this important improvement, it is evident that a PNLSS model that describes the nonlinear dynamics observed in the measured data has been successfully implemented without imposing any prior knowledge about the nonlinearities in the measured data.

4.4.2. Identifying a Parsimonious Data Driven PNLSS Model

Although the results achieved in section 4.4.1 indicated high degree of accuracy where the full identified PNLSS model was able to capture the nonlinear phenomena observed in the measured data, the total number of the estimated parameters for the identified model is 13728. The large number of estimated parameters can be narrowed down to the order of the polynomial degree which was used for the full PNLSS model. In addition, the combination of both even and odd monomial degrees in developing a suitable PNLSS model can be disadvantageous for some cases where the nonlinear phenomena exhibited by the system are dominated by either even or odd polynomial degrees. Hence, in this section, a study on identifying a suitable PNLSS model using a series of different reduced monomial combinations is conducted. The aim is to develop the best PNLSS model with the lowest number of parameters capable of modelling the nonlinearities observed in the measured data of the aero-engine casing. Seven different 6th-order PNLSS models were developed based on the monomial combination shown in Table 2. The same sine sweep data at 100N were utilised as the data set for the estimation of each PNLSS model while another set of sine sweep data at 50N was used for the validation of each estimated PNLSS model. Each monomial combination simulation experiment was based on measured sine sweep data with signal sample sizes of 1474561×1 for the input and 1474561×2 for the output. The signal sizes are based on the Single Input Multiple Output (SIMO) configuration which is being considered in this paper. As quality measures, the relative RMS error in the time and frequency domain and the NRMSE of each successful iteration of the LM optimisation were computed for each estimated PNLSS model. The performance of each simulated PNLSS model structure in Table 2 is calculated based on the following expression:

$$\mathrm{NRMSE} = \frac{\sqrt{\frac{1}{N_\mathrm{t}}\sum_{t=1}^{N_\mathrm{t}}(y_\mathrm{model}(t) - y_\mathrm{measured}(t))^T(y_\mathrm{model}(t) - y_\mathrm{measured}(t))}}{\sqrt{\frac{1}{N_\mathrm{t}}\sum_{t=1}^{N_\mathrm{t}}(y_\mathrm{measured}(t))^T(y_\mathrm{measured}(t))}} \tag{25}$$

where y_model and y_measured are the PNLSS output and measured output, while N_t is the total number of data points. Transforming the error to the frequency domain was also another criterion used in judging the performance of each simulated monomial degree combination, the amplitude plot of the frequency domain error helps to show in which frequency bands the model performs well, and in which frequency bands it performs poor.

Table 3: Estimation results for different monomial combination experiments

Polynomial Degrees	Estimation RMS Error (%)	Total Number of Parameters	Simulation Time (Hours)
2-3	15.91	672	8.37
2-3-4-5	4.89	3696	41.52
2-3-4-5-6-7	1.72	13728	121.29
2-4	16.04	1232	11.74
2-4-6	11.87	4928	63.81
3-5	5.01	2520	34.26
3-5-7	1.58	8856	101.65

Figure 12 shows the time and frequency domain error plots obtained for two PNLSS simulation results out of the seven PNLSS simulations that were conducted. For all the different PNLSS models that were estimated, the RMS error of the time and frequency domain is seen to decrease for increasing model complexity, in particular within the frequency band where nonlinear distortions are observed as shown in Figure 12 and Figure 14. The estimation errors for each PNLSS simulated model are presented in Table 3 with an approximate value of the time taken to compute each simulated PNLSS model.

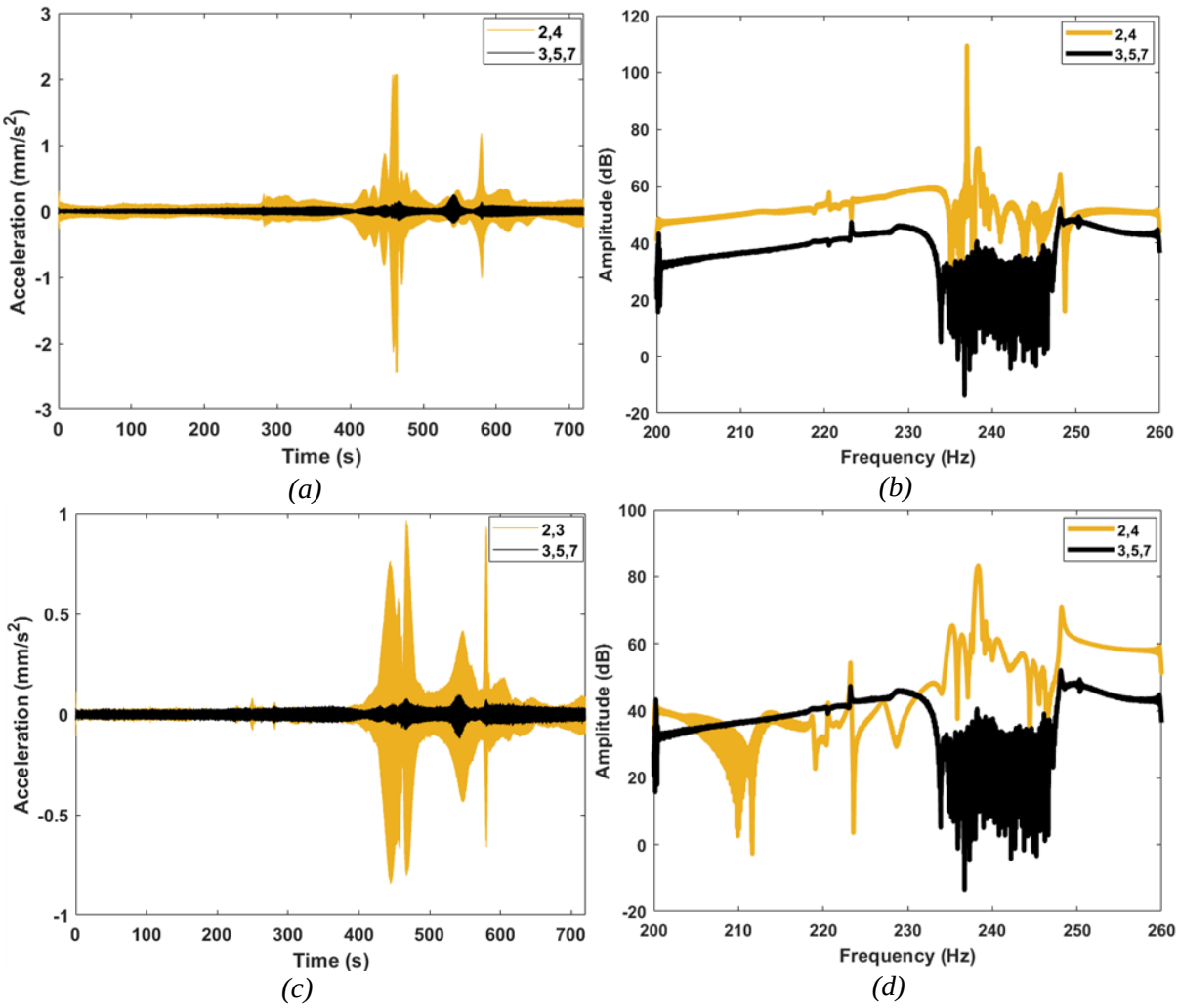

Figure 12: Time and Frequency domain estimated model error for simulated PNLSS model using monomial combination of 2,4 and 3, 5,7: a (time domain error of the drive point), b (frequency domain error of the drive point), c (time domain error of Mnode), d (frequency domain error of Mnode).

The lowest RMS error value of 1.58% is achieved for the monomial combination of the order (3, 5, and 7) as shown in Table 3. In addition, judging from the time and frequency domain error comparisons in Figure 12, it is possible to conclude that the monomial combinations with odd degrees can be used to produce better fitting PNLSS models compared to the PNLSS model with even monomial degree combination. In terms of obtaining a parsimonious model, Table 3 shows how the effect of increasing the complexity of the monomial degrees can cause a drastic growth in the total number of parameters estimated by each PNLSS model. In this case, a parsimonious model is defined as a monomial combination with the lowest RMS percentage error value between the PNLSS models and the measured data whilst using the least number of parameters or variables to obtain the best prediction. From a performance perspective, selecting the monomial degrees 3, 5, and 7 yields the estimation error of 1.58 % with the total number of 8856 estimated parameters.

Compared to the identified PNLSS model with monomial combination of 2-3-4-5-6-7 and 13728 parameters, which took just over 5 days on a standard desktop to complete all the computations, one can conclude that a PNLSS model with monomial degrees of 3-5 or 3-5-7 can be used to correctly reproduce or model the nonlinearities observed in the measured data to a high degree of accuracy. Using either of these two proposed PNLSS model configurations has not only shown an advantage in terms of obtaining a reasonable parsimonious model, the computational burden and time involved in minimising the cost functions for these two models were considerably lower than the initial identified PNLSS model in Figure 11. Figure 13 shows the behaviour of the NRMSE for all simulated PNLSS

cases, it is worth stating that for Figures 13 and 16, there are more than 120 Levenberg-Marquardt iterations completed. However, only the successful iterations (i.e. the iterations for which the cost function decreased during the optimisation process) are plotted.

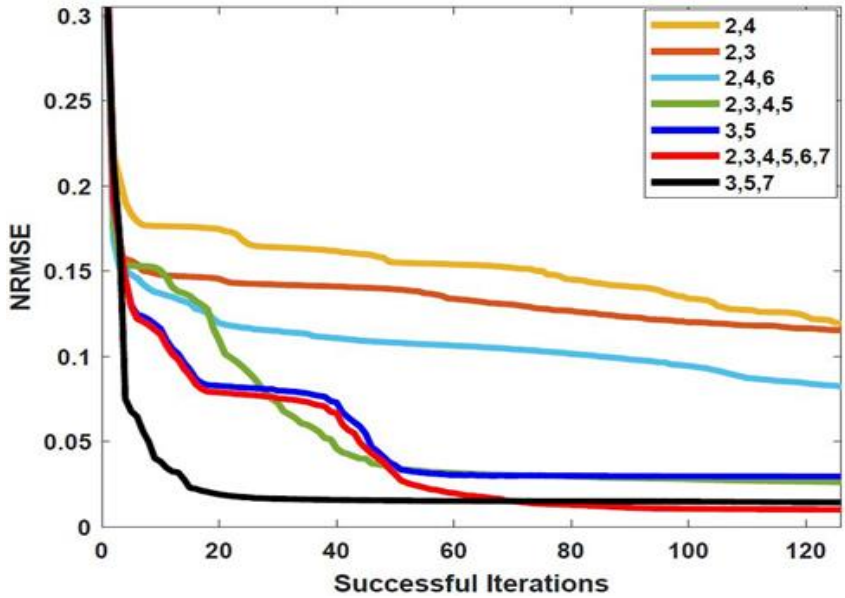

Figure 13: NRMS estimation error over successful Levenberg-Marquardt iterations for the seven simulated PNLSS models based on different monomial degree combinations.

By plotting the normalised root mean squared error against the successful iterations of the LM optimisation, it is also possible to get useful information on the monomial degree combination that produces the best PNLSS model capable of modelling the nonlinearities based on the error magnitude and convergence rate during optimisation. From Figure 13, the NRMSE with odd monomial degrees generally show significantly better and faster convergence compared to the ones with even and odd monomial degree combinations. The model with monomial degrees 3, 5, and 7 reaches the second best NRMSE after the full model with monomial degrees 2, 3, 4, 5, 6, and 7, but it converges faster and uses significantly less parameters. Since the obtained NRMSE values for both models are fairly close, the model with monomial degrees 3, 5, and 7 is retained because of the trade-off between the performance and parameter parsimony as illustrated in the results presented in Table 3.

Comparing the measured data and the simulated PNLSS model in the time domain for monomial degree 3-5-7 as shown in Figure 14, it is evident that the model was practically able to accurately reproduce the maximum amplitude of each mode in the envelope of the time series. In Figure 14b and 15d, the simulated PNLSS model was able to replicate correctly the frequency spectrum and also the characteristics for each considered nonlinear mode of the measured data. The nonlinear distortions observed in the envelope of the time series at higher excitation level was also well captured by the simulated PNLSS model as shown in Figure 14a and 14c. Based on all these observations it is possible to draw a conclusion that the nonlinearities observed during the experimental campaign of the aero-engine casing assembly are best modelled using the polynomial representation with odd degrees. Both, the error values and the LM iteration curves demonstrate how useful the PNLSS models can be when modelling the nonlinearities observed in the experimental data without prior assumptions.

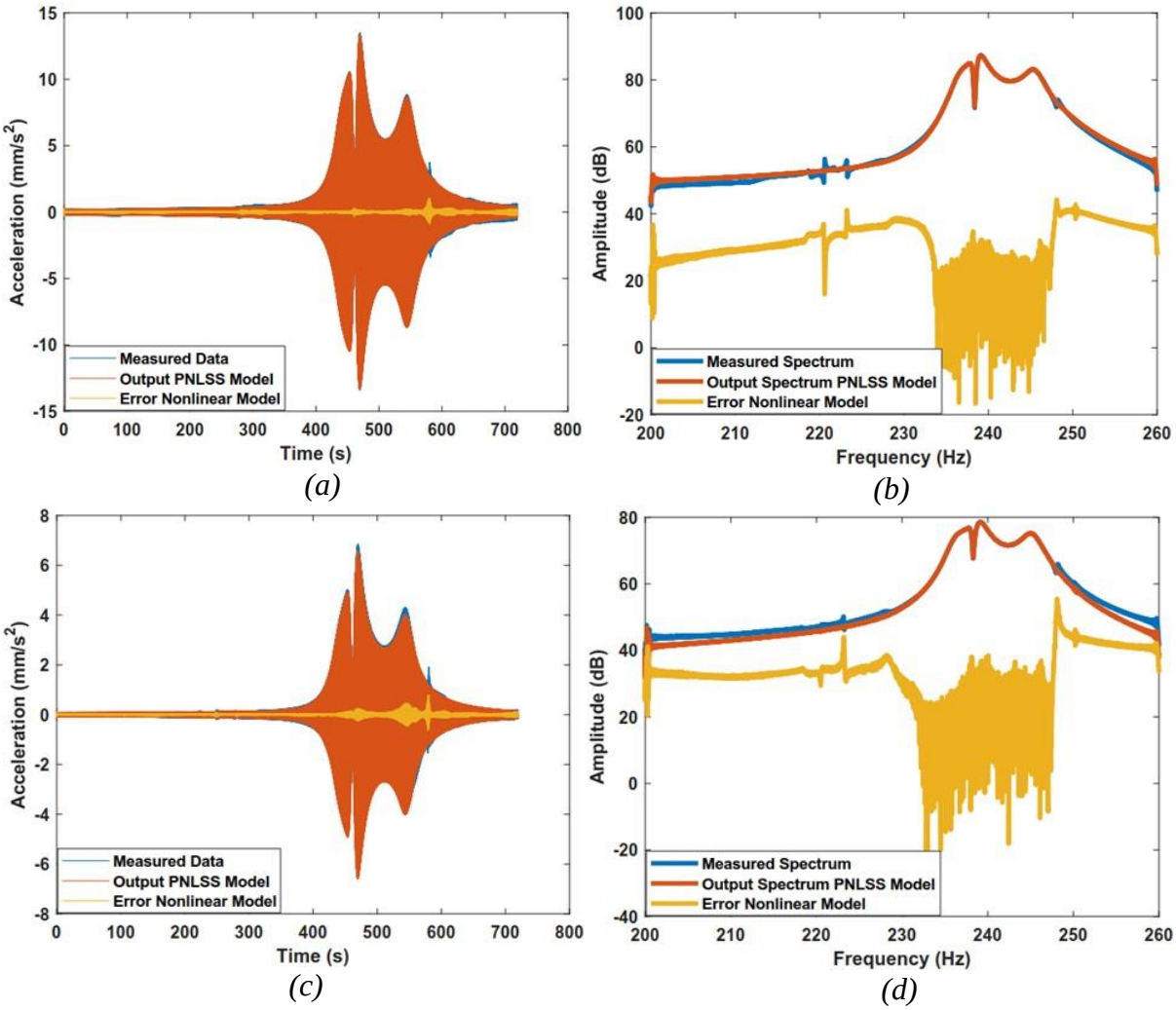

Figure 14: Time and Frequency domain comparison of the best estimated PNLSS model against measured data based on polynomial order 3, 5 and 7: a (Time domain response of the drive point),b (Frequency domain response of the drive point) c (Time domain response of Mnode 2), d (Frequency domain response of Mnode 2).

Most importantly, this section of the paper has also shown some advantages and the possibility of obtaining an optimal parsimonious model suitable for modelling the nonlinearities with a low percentage error by running several simulation studies using different monomial degree combinations.

4.5. PNLSS Model Validation Under Sine-Sweep and Broadband Excitations

To examine the domain of validity for the different simulated PNLSS models, each model is subjected to a validation experiment by introducing new measured data. In the estimation step, the models obtained after a successful Levenberg-Marquardt iteration are retained as candidate models. In the validation step, the model among the candidate models that achieves the lowest cost on the validation data is selected as the final model. Note that there is no optimization in this validation step (no computation of Jacobians, step sizes, et cetera), just an evaluation of all the candidate models by simulating the candidate models with the validation input and comparing the measured validation output with the simulated output. The validation experiment was intended to measure the performance of the identified PNLSS models under similar practical conditions based on the frequency and amplitude range of interest. However, since the system under consideration is nonlinear, then in this validation stage, it is advisable to use experimental data with lower excitation levels to avoid extrapolation. In this case, the measured sine-sweep data at 50N were introduced to each identified PNLSS model in Table 3. The RMS error in the time and frequency domain were used as quality measures to judge the performance

of each validation experiment. Seven different PNLSS model validation experiments were conducted and a comparison between the measured data and the reconstructed PNLSS model at excitation level of 50N was used to visualise the performance of each validation experiment.

Table 4: Validation results for different monomial combination experiments

Polynomial Degrees	Validation Error (%)
2-3	10.83
2-3-4-5	4.71
2-3-4-5-6-7	1.67
2-4	11.69
2-4-6	6.34
3-5	2.13
3-5-7	1.44

The percentage error of the nonlinear PNLSS model for each validation experiment is illustrated in Table 4, where the RMS errors for the validation experiment were generally lower than the errors for the estimation results.

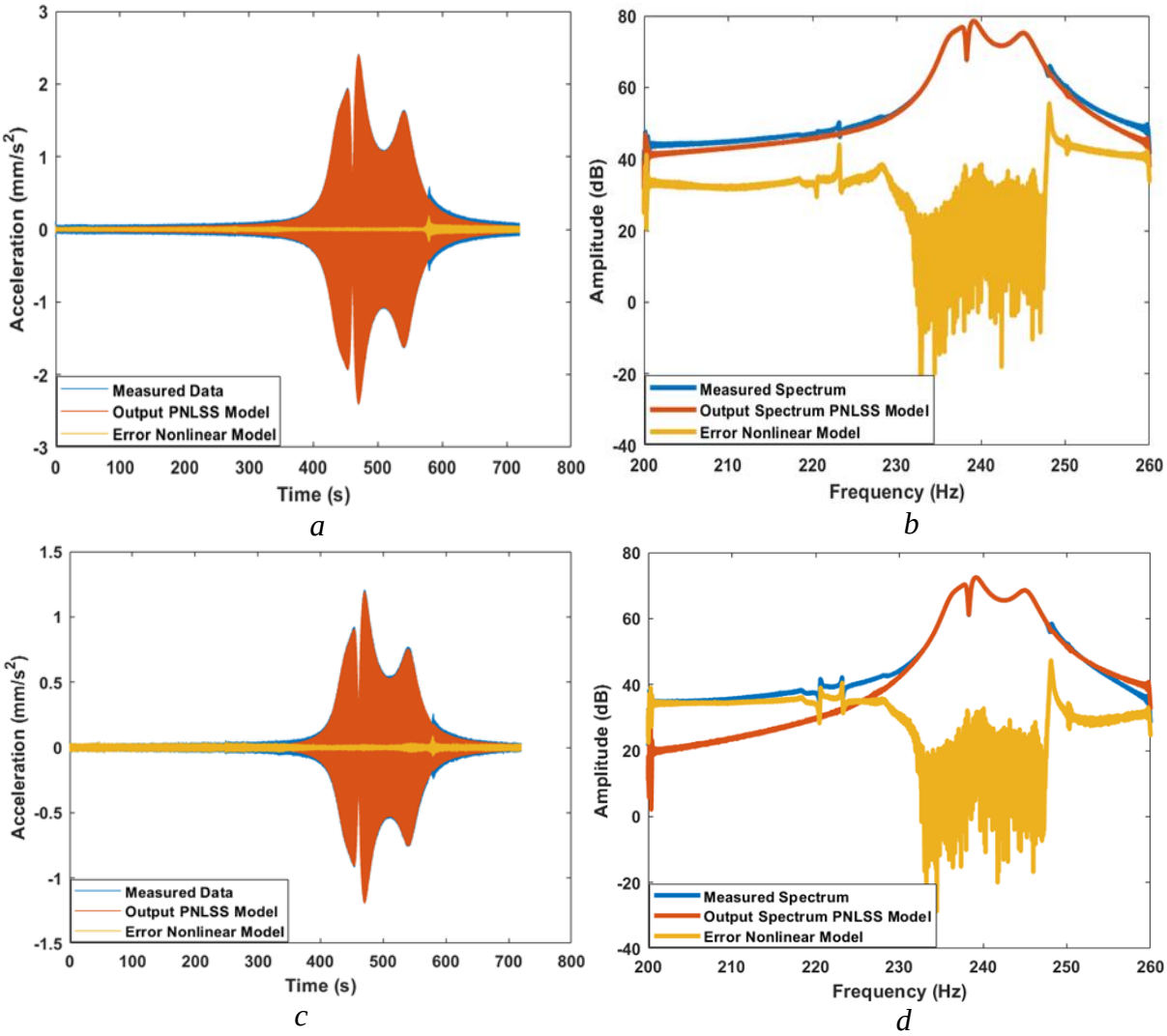

Figure 15: Validation of PNLSS model against measured data for 3-5-7 monomial combinations. a (Time domain response of the drive point), b (Frequency domain response of the drive point) c (Time domain response of Mnode 2) d (Frequency domain response of Mnode 2).

As shown in the table, amongst all the PNLSS models in the validation study, the PNLSS model with the monomial degrees of 3-5-7 has the lowest RMS error value. Figure 15 illustrates the corresponding time series envelope and the spectrum for this PNLSS model compared with experimental data at 50N for two different locations on the aero-engine casing. The PNLSS results presented in Figure 15 show good agreement with the measured data, in particular around the regions of the three dominant resonance peaks.

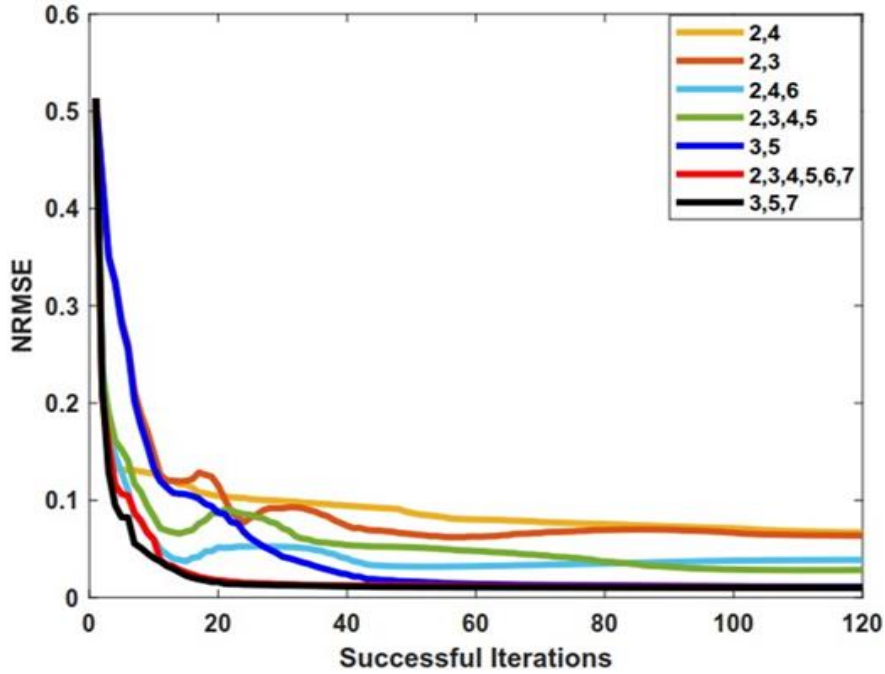

Figure 16: NRMS validation error over the successful Levenberg-Marquardt iterations for the seven simulated PNLSS models based on different monomial degree combinations.

Although minor discrepancies are still observed between the PNLSS model and measured data, these discrepancies are outside the resonances and frequencies of interest and can be narrowed to errors generated from the flexibility of the PNLSS models. Similar to the identification results, the normalised root mean squared error (NRMSE) for the evolution of the candidate models was plotted for each model in the validation study. Results of the NRMSE curve for the seven validation models are illustrated in Figure 16. For all the models, the final NRMSE is less than 10%, indicating that the PNLSS model structure represents a reasonable representation of the nonlinear dynamics of the aero-engine casing. Moreover, the NRMSE reaches near optimum only after 20 iterations. The performance of the model is thus robust to the model selection process as it does not seem to matter too much which of the model realisations between iterations 20 and 120 actually gets selected as the best one on the estimation data.

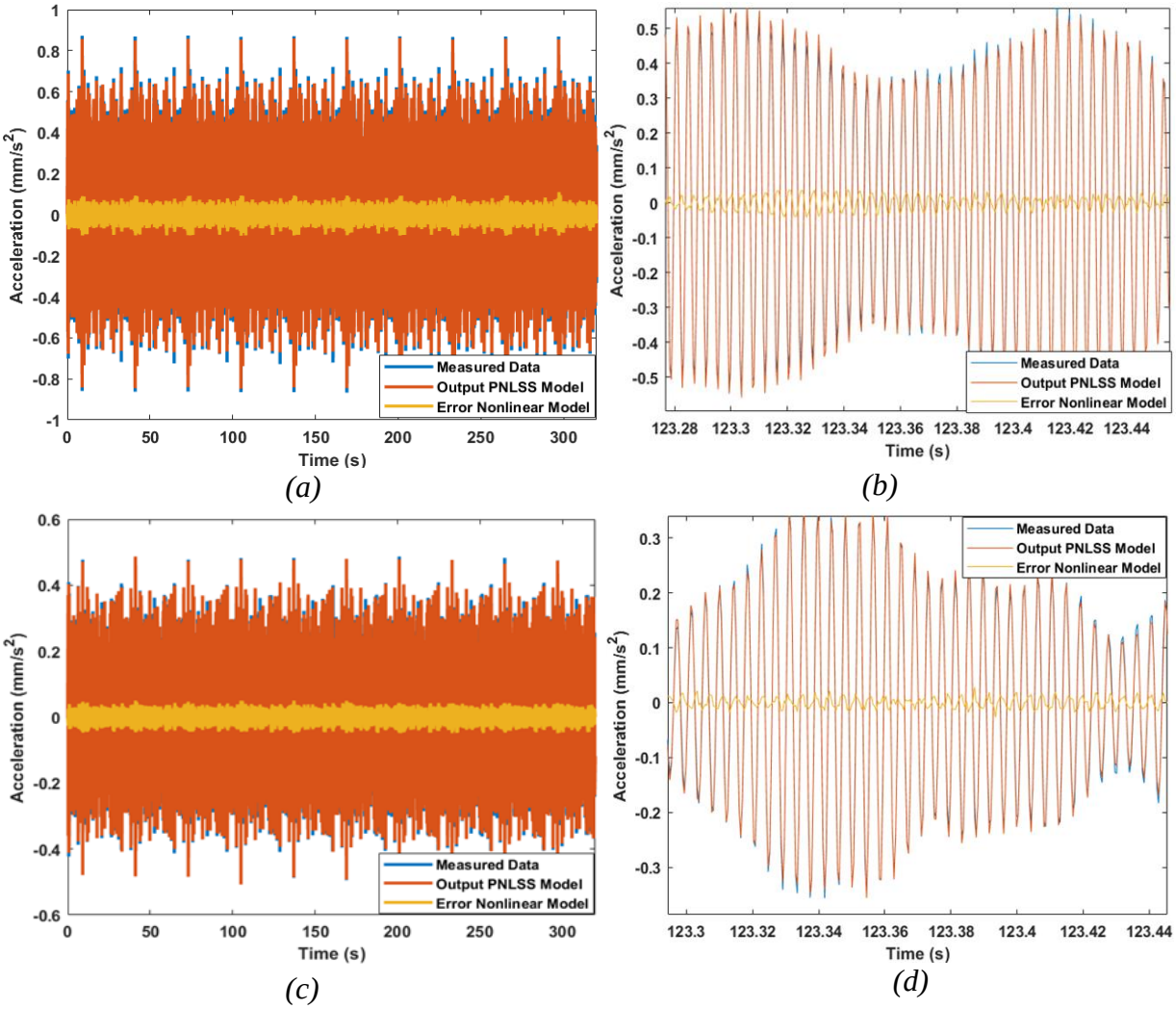

Figure 17: Time-domain performance of the validated model for the monomials of degree 3-5-7 based on the measured broadband data. a (Time domain response of the drive point), b (Zoomed-in time domain response of the drive point), c (Time domain response of Mnode 2) d (Zoomed-in time domain response of Mnode 2).

To further test the domain of validity of the best performing PNLSS model, the PNLSS model was subjected to another validation test. In this case, the broadband data measured at 40N RMS excitation level was introduced to the PNLSS model with the monomial degree combinations of (3-5-7). Figure 17 shows a short window time domain comparison of the measured and predicted data by the optimal PNLSS model. The RMS value of the error on this validation data set is $0.05mm/s^2$. Figure 17 agreeably demonstrates the significance and validity of the PNLSS model using a different type of excitation signal, where the achieved small RMS value indicates the predictive confidence of the PNLSS model with the monomial degree combinations of (3-5-7). From a user point of view, having minor errors between the measured data and the reconstructed PNLSS models is in many cases acceptable, given that a good estimate of the maximum amplitude, the frequency of the response and other important features of the predicted responses are obtained. Most importantly, for this black-box application, the results have shown a good degree of accuracy based on the various error measures discussed in this work. Finally, it is also worth stating that a price to pay for the large modelling flexibility achieved in this case of nonlinear state space models is the presence of systematic and variance errors which are sometimes unavoidable depending on the problem which is being investigated.

5. Conclusion

In this paper, a black-box identification method has been used to gain useful insights into the nonlinearities observed in an aero-engine casing during an experimental campaign. A discrete-time PNLSS model was used for the identification and validation of the nonlinear phenomena observed in the measured data obtained from the vibration tests conducted on a large aerospace structure. The PNLSS models were investigated using the sine-sweep data. The full PNLSS model was initialised using the Best Linear Approximation and a Local Polynomial Method for local smoothing of the FRFs. Subsequently, a weighted least-square minimisation approach was used to identify the PNLSS model parameters in the time domain. The success of the PNLSS model was judged based on the RMS and NRMSE error measures between the data simulated from the PNLSS model and the true measured data. Based on the achieved RMS values of 1.58% and 1.44% obtained from the identification and validation models respectively, one can conclude that the PNLSS method was able to successfully model the nonlinear dynamics observed in the measured data without any prior knowledge or physical insight to the nature of the nonlinearities. Several drawbacks are associated with polynomial nonlinear state space application, one of which is the explosive behaviour of polynomials outside the estimated region. A polynomial tends to attain large numerical values when its arguments are large, compared to the behaviour of other basis functions when used in similar application. However, it should also be noted that extrapolating with an estimated model is generally never a good idea for nonlinear systems. To overcome the limitation of the great number of parameters involved in the construction of the multivariate polynomials, tensor techniques can be used to prune the nonlinear parameters in the state space identification. Based on linearisations of the multivariate polynomial in a PNLSS model and a tensor decomposition, the nonlinear functions $E\zeta(x(t), u(t))$ and $F\eta(x(t), u(t))$ in the state space equation can be represented by decoupled polynomials [19]. This representation further helps to reduce the number of parameters to be estimated by removing the cross-terms in the multivariate polynomials. In summary, results presented in this paper have shown the strength of using a black-box method to model the nonlinearities observed in a large aerospace structure.

Acknowledgment

This work was funded by the Engineering and Physical Science Research Council (EPSRC) in the UK, Rolls Royce, the European Research Council (ERC), the Swedish Research Council (VR), and the Swedish Foundation for Strategic Research (SSF): Samson.B. Cooper is supported by EPSRC grant EP/L505365/1. Koen Tiels is supported by ERC Grant Agreement n.320378, VR project NewLEADS with contract number 621-2016-06079, and SSF project ASSEMBLE with contract number RIT15-0012. All financial support are gratefully acknowledged.

Reference

1. J.P.Noël and G.Kerschen, *Nonlinear system identification in structural dynamics: 10 more years of progress.* Mechanical Systems and Signal Processing, 2017. **83**: p. 2-35.

2. J.P.Noël, et al. *Nonlinear dynamic analysis of an F-16 aircraft using GVT data*. in *In Proceedings of the International Forum on Aeroelasticity and Structural Dynamics (IFASD)*. 2013. Bristol.

3. J.R.Ahlquist, et al. *Assessment of Nonlinear Structural Response in A400M GVT*. in *in Proceedings of the 28th International Modal Analysis Conference (IMAC)*. 2010. Jacksonville, Florida: Springer.

4. U.Fuellekrug and D.Goege, *Identification of weak non-linearities within complex aerospace structures.* Aerospace Science and Technology, 2012. **23**(1): p. 53-62.

5. S.B.Cooper, D.DiMaio, and D.J.Ewins, *Integration of system identification and finite element modelling of nonlinear vibrating structures.* Journal of Mechanical Systems and Signal Processing, 2017. **102**: p. 401-430.

6. D.J.Ewins, B.Weekes, and A.DelliCarri, *Modal Testing for Model Validation of Structures with Discrete Nonlinearities.* Journal of Philosophical Transaction, 2015. **373**: p. 1-20.

7. G.Kerschen, et al., *Past, present and future of nonlinear system identification in structural dynamics.* Mechanical Systems and Signal Processing, 2006. **20**(3): p. 505-592.

8. V.Ondra, I.A.Sever, and C.W.Schwingshackl, *A method for detection and characterisation of structural non-linearities using the Hilbert transform and neural networks.* Mechanical Systems and Signal Processing, 2017. **83**: p. 210-227.

9. J.P.Noël, et al., *Grey-box identification of a non-linear solar array structure using cubic splines.* International Journal of Non-Linear Mechanics, 2014. **67**: p. 106-119.

10. Q.Chen, et al., *Genetic algorithm with an improved fitness function for (N)ARX modelling.* Mechanical Systems and Signal Processing, 2007. **21**(2): p. 994-1007.

11. Z.K.Peng, et al., *Feasibility study of structural damage detection using NARMAX modelling and Nonlinear Output Frequency Response Function based analysis.* Mechanical Systems and Signal Processing, 2011. **25**(3): p. 1045-1061.

12. A.A.Khan, N.S.Vyas., *Non-linear Parameter Estimation Using Volterra And Wiener Theories.* Sound and Vibration, 1998. **221**: p. 805-821.

13. A.A.Khan, N.S.Vyas., *Nonlinear bearing stiffness parameter estimation in flexible rotor-bearing systems using Volterra and Wiener approach.* Probabilistic Engineering Mechanics, 2000. **16**: p. 137-157.

14. I.Tawfiq and T.Vinh, *Contribution to the Extension of Modal Analysis to Non-Linear Structure Using Volterra Functional Series.* Mechanical Systems and Signal Processing, 2003. **17**(2): p. 379-407.

15. L.Facchini, M.Betti, and P.Biagini, *Neural network based modal identification of structural systems through output-only measurement.* Computers & Structures, 2014. **138**: p. 183-194.

16. J.Paduart, et al., *Identification of nonlinear systems using Polynomial Nonlinear State Space models.* Automatica, 2010. **46**(4): p. 647-656.

17. J.P.Noël, et al., *A nonlinear state-space approach to hysteresis identification.* Mechanical Systems and Signal Processing, 2017. **84**: p. 171-184.

18. A.Svensson and T.B.Schön, *A flexible state–space model for learning nonlinear dynamical systems.* Automatica, 2017. **80**: p. 189-199.

19. A.Fakhrizadeh Esfahani, et al., *Parameter reduction in nonlinear state-space identification of hysteresis.* Mechanical Systems and Signal Processing, 2018. **104**: p. 884-895.

20. R.Relan, et al., *Data driven discrete-time parsimonious identification of a nonlinear state-space model for a weakly nonlinear system with short data record.* Mechanical Systems and Signal Processing, 2018. **104**: p. 929-943.

21. J.Decuyper, et al., *Nonlinear state-space modelling of the kinematics of an oscillating circular cylinder in a fluid flow.* Mechanical Systems and Signal Processing, 2018. **98**: p. 209-230.

22. R.Pintelon, et al., *Estimation of nonparametric noise and FRF models for multivariable systems—Part I: Theory.* Mechanical Systems and Signal Processing, 2010. **24**(3): p. 573-595.

23. R.Pintelon, *Frequency-domain subspace system identification using non-parametric noise models.* Automatica, 2002. **38**: p. 1295-1311.

24. D.W.Marquardt, *An Algorithm for Least-Squares Estimation of Nonlinear Parameters* Society for Industrial and Applied Mathematics 1963. **11**(2): p. 431-441.

25. J.Schoukens, T.Dobrowiecki, and R.Pintelon, *Parametric and nonparametric identification of linear systems in the presence of nonlinear distortions-A frequency domian approach.* IEEE Transactions on Automatic Control, 1998. **43**(2): p. 176-190.

26. R.Pintelon and J.Schoukens, *System Identification: A Frequency Domain Approach*. 2012: Wiley-IEEE Press.

27. J.Schoukens, et al., *Nonparametric Preprocessing in System Identification: a Powerful Tool.* European Journal of Control, 2009. **15**(3-4): p. 260-274.

28. T.P.Dobrowiecki and J.Schoukens, *Linear Approximation of Weakly Nonlinear MIMO Systems.* IEEE Transactions on Instrumentation and Measurement, 2007. **56**(3): p. 887-894.

29. R.Pintelon, et al., *Estimation of nonparametric noise and FRF models for multivariable systems—Part II: Extensions, applications.* Mechanical Systems and Signal Processing, 2010. **24**(3): p. 596-616.

30. T.Glad and L.Ljung, *Control Theory Multivariable and Nonlinear Methods* 2000, London: Taylor and Francis. 477.

31. B.Titurus and M.I.Friswell. *Regularisation in model updating.* International Journal of Numerical methods in Engineering, 2008. **75**: p. 440-478.

32. S.B.Cooper, et al. *An Experimental Case Study for Nonlinear Model Validation: Effects of Nonlinearities in an Aero-Engine Structure*. in *35th International Modal Analysis Conference (IMAC)*. 2018. Orlando, Florida: Society for Experimental Mechanics.

33. B.Peeters, et al., *The PolyMAX frequency-domain method: A new standard for modal parameter estimation.* Shock and Vibration, 2004. **11**(3-4): p. 395-409.

34. B.Weekes and D.Ewins, *Multi-frequency, 3D ODS measurement by continuous scan laser Doppler vibrometry*. Mechanical Systems and Signal Processing, 2015. **58-59**: p. 325-339.

35. T.McKelvey, H.Akçay, and L.Ljung, *Subspace-based Multivariable System Identification from Frequency Response Data.* IEEE Transactions on Automatic Control, 1996. **41**(7): p. 960-979.